



Surface modified C, O co-doped polymeric g-C₃N₄ as an efficient photocatalyst for visible light assisted CO₂ reduction and H₂O₂ production

Subhajyoti Samanta^a, Rajkumar Yadav^{b,c}, Abhinav Kumar^a, Anil Kumar Sinha^{b,c,*},
Rajendra Srivastava^{a,*}

^a Department of Chemistry, Indian Institute of Technology Ropar, Rupnagar 140001, Punjab, India

^b BioFuels Division, CSIR-Indian Institute of Petroleum, Dehradun 248005, India

^c Academy of Scientific and Innovative Research (AcSIR), New Delhi, India

ARTICLE INFO

Keywords:

C, O-doping
Carbon nitride
Visible light photocatalysis
CO₂ photoreduction
H₂O₂ production
O₂ reduction

ABSTRACT

Mimicking the artificial photosynthesis utilizing solar energy for the production of hydrocarbon fuel is a sustainable strategy to tackle the fossil fuel-based energy crisis. Herein, a surface-modified g-C₃N₄ was synthesized by the co-condensation of urea + thiourea and 2-methyl imidazole. Physicochemical characterizations reveal that O and C are co-doped, as evident by the XPS and solid-state NMR spectroscopy. The light absorption edge is red shifted, lifetimes of the charge carriers, and electron injection efficiencies are ameliorated appropriately. Photocatalysts are employed in the CO₂ reduction (from TEOA dissolved water + CO₂ gas mixture) and H₂O₂ production (from pure H₂O and O₂ in absence of any organic electron/proton donor) without involving any co-catalyst. CO₂-adsorption/TPD measurements support the higher CO₂ uptake and lower adsorption energy after the surface modification as confirmed from DFT calculation. Mott-Schottky and VBXPS confirm that C, O co-doping bring required thermodynamic potential that facilitates the CO₂/CH₃OH and O₂/H₂O₂ reactions.

1. Introduction

Efficient utilization of solar energy for the production of value-added chemical is a tremendously growing research area considering the limited fossil fuel feedstock [1–4]. In this direction, conversion of greenhouse gas CO₂ into various hydrocarbon products by employing solar radiation and photocatalyst is need of the hour. This conversion process is much-needed replacement of the conventional industrial process operated at high temperature/pressure for CO₂ to methanol conversion reaction and the reverse water gas shift reaction [5,6]. The very first effort towards this target has been pioneered by Inoue et al. employing semiconductor photo electrocatalyst in aqueous solution [7]. Similarly, sunlight-driven direct conversion of H₂O and O₂ into H₂O₂ is a challenging task, and it is conventionally produced by anthraquinone/Pd based catalytic system or noble metal Au-Pd based catalysts employing H₂ as the reactant. However, these processes have some serious disadvantages like solvent separation, extraction, regeneration of 2-alkylanthraquinone (AQ) to anthrahydroquinone (AHQ), the involvement of high energy input and most importantly the involvement of highly explosive H₂ gas [8,9]. As an alternative, the direct conversion of H₂O to H₂O₂ involving semiconductor photocatalyst is a sustainable catalytic pathway. The first breakthrough has

been pioneered by Kormann et al. in which researchers have employed TiO₂ photocatalyst to produce H₂O₂ from the O₂ dissolved aqueous-alcoholic (as proton donor) solution [10]. This reaction proceeds via the oxidation of alcohols by the photo-induced holes which produce protons that subsequently convert into H₂O₂ by the light-induced electrons with the help of dissolved O₂ ($R-CH_2OH + h^+ = R-CHO + 2H^+$; $O_2 + 2H^+ + 2e^- = H_2O_2$) [11]. However, the one-electron reduction of O₂ to (·OOH) radicals restricts the selectivity of the desired product which ends up with the endo-peroxide species [11]. Therefore, the selective two electrons reduction involving H₂O and O₂ for the synthesis of H₂O₂ with 100% atom economy under visible light irradiation is a challenging task [11]. Also, it nullifies the requirement of alcohols as proton source for this purpose. In this process, H₂O is oxidized by the light-induced holes to produce O₂ and H⁺ ($2H_2O + 4h^+ = O_2 + 4H^+$) which again selectively reduce by the light-induced two electrons leading to the H₂O₂ formation ($2H^+ + 2e^- + O_2 = H_2O_2$) [11]. This is a highly confronting job because there is a high possibility for the one-electron reduction of O₂ to produce superoxide radicals and also the simultaneous utilization of holes and electrons to facilitate the desired production of H₂O₂, especially in the absence of any proton donor or co-catalyst.

To address these challenges, heterogeneous semiconductor

* Corresponding authors.

E-mail addresses: asinha@iip.res.in (A. Kumar Sinha), rajendra@iitpr.ac.in (R. Srivastava).

<https://doi.org/10.1016/j.apcatb.2019.118054>

Received 26 April 2019; Received in revised form 31 July 2019; Accepted 3 August 2019

Available online 08 August 2019

0926-3373/ © 2019 Elsevier B.V. All rights reserved.

photocatalysts like metal oxides, metal sulfides, metal phosphides, polyoxometalate (POM), polymeric organic semiconductors, metal-organic framework (MOF) based materials, and carbonaceous materials have been investigated over the last few years [12–18]. Interestingly, most of the studies are focused on metal oxides such as TiO_2 and its composite photocatalysts, which exhibited remarkable catalytic activity for CO_2 photoreduction reactions [19–21]. However, Among these photocatalysts, one of the most emerging photocatalysts, graphitic carbon nitride ($\text{g-C}_3\text{N}_4$), is being extensively investigated for both the reactions owing to its appropriate band alignments required to trigger these reactions, effective visible light absorption with high extinction coefficient, high thermal and physical stability, and most importantly the facile synthesis recipe [22–27]. Graphitic carbon nitride ($\text{g-C}_3\text{N}_4$) having a band gap of 2.7 eV is actually built-up from the thermal condensation of various carbon and nitrogen-containing organic moieties leading to the construction of melem framework which again polymerizes and bridge through the uncondensed amino groups resulting in the formation of graphitic nitride moiety [28]. This polymeric material contains $\text{N-C}=\text{N}$ basal plane, which can bind CO_2 molecule and also force CO_2 molecule for partial bending through the N-lone pair donation to the LUMO of ' $\text{C}=\text{O}$ ' bond of CO_2 molecule. On the other hand, it can suppress the one electron reduction of O_2 to form ($\cdot\text{OOH}$) radicals due to the rapid formation of '1,4-endoperoxide' species localized at the 'C1-N4' position of melem unit promoting the two-electron reduction to produce H_2O_2 [11]. However, bulk $\text{g-C}_3\text{N}_4$ suffers from some serious limitations like rapid charge carrier recombination, low light absorption capacity, and extremely low specific surface area ($\sim 10\text{ m}^2/\text{g}$) that hinder its photocatalytic efficiency [28,29]. These factors restrict the lower selectivity for the two electrons reduction of O_2 and low CO_2 uptake capacities. These bottlenecks can be further improved by surface modification via intrinsic doping which can tailor the specific surface area, extend the light absorption capability and separate the charge carriers effectively by minimizing the nonradiative recombination tendencies [29]. Several strategies have been put forward to address these issues, such as doping with heteroatoms (S, N, O, P, etc.), vacancy creation, defect engineering, thermal etching, liquid-phase exfoliation, precursors alteration, band gap tuning, morphology tuning, and so on [30–35]. Fu et al. reported that O-doped tube shape $\text{g-C}_3\text{N}_4$ exhibited better CO_2 photoreduction activity than the bulk $\text{g-C}_3\text{N}_4$ [32]. Liu et al. reported that P-doped amino-rich $\text{g-C}_3\text{N}_4$ displayed enhanced CO_2 capture and photoreduction reaction with high product selectivity [33]. Wang et al. reported that S-doped $\text{g-C}_3\text{N}_4$ exhibited better CO_2 photoreduction activity [30]. Recently, Vidyasagar et al. reported that C-doped $\text{g-C}_3\text{N}_4$ by phenyl grafting had shown better CO_2 photoreduction activity [36]. Again, nitrogen-vacancy enriched $\text{g-C}_3\text{N}_4$ [31], pyromellitic diimide (PDI) incorporated $\text{g-C}_3\text{N}_4$ [12], melitic triimide-doped carbon nitride [37], biphenyl diimide doped $\text{g-C}_3\text{N}_4$ [38], benzene substituted $\text{g-C}_3\text{N}_4$ [39], have shown enhanced H_2O_2 production reaction via two-electron reduction pathway. A recent study reported the *in-situ* photogenerated H_2O_2 over $\text{g-C}_3\text{N}_4$ for aromatic compounds degradation [40]. Very recently several non-metals, especially O and C doped $\text{g-C}_3\text{N}_4$ was reported for different photocatalytic applications which ultimately indicated that doping with non-metals leading to the intrinsic surface modification is an alternative strategy to fine-tune the photocatalytic activity of bulk $\text{g-C}_3\text{N}_4$ further [41–47]. Among these non-metal dopants, C-doping in $\text{g-C}_3\text{N}_4$ could promote the electron conductivity and enhance the photogenerated charge carrier dissociation effectively which is important for improving the photocatalytic activity while O doping might be extending the light-harvesting domain and also can facilitate the adsorption of the reactant molecules on the catalyst's surface. Thus, these literature reports conclude that intrinsic surface modification of $\text{g-C}_3\text{N}_4$ with non-metals doping has the ability to emulate the CO_2 reduction and selective two electrons reduction of O_2 to produce H_2O_2 .

Herein, O and C co-doped $\text{g-C}_3\text{N}_4$ was synthesized to enhance the CO_2 capture capability of the bulk $\text{g-C}_3\text{N}_4$. The optimum quantity of 2-

methyl imidazole (2-MI, an organic linker dopant) was co-condensed at high temperature with urea and thiourea (as a bulk $\text{g-C}_3\text{N}_4$ precursor) to enhance the basicity, visible light absorption capacity, and surface area of the material and minimize the recombination tendency of the charge carriers. The resulting photocatalyst was employed for CO_2 photoreduction in aqueous 'suspension medium', and H_2O_2 production from O_2 dissolved water. Detailed photocatalytic investigation reveals that CO_2 reduction leads to the selective synthesis of methanol which was confirmed from the *in-situ* FTIR analysis. Upon 2-MI modification of the bulk $\text{g-C}_3\text{N}_4$, the CO_2 binding energy was lowered that facilitated the CO_2 reduction reaction which was further supported by DFT calculation. Further, H_2O_2 was synthesized from H_2O and O_2 under visible light following a two-electron reduction pathway. The structure-activity relationship was established using in-depth physicochemical and photoelectrochemical measurements and various control reactions and scavenging studies.

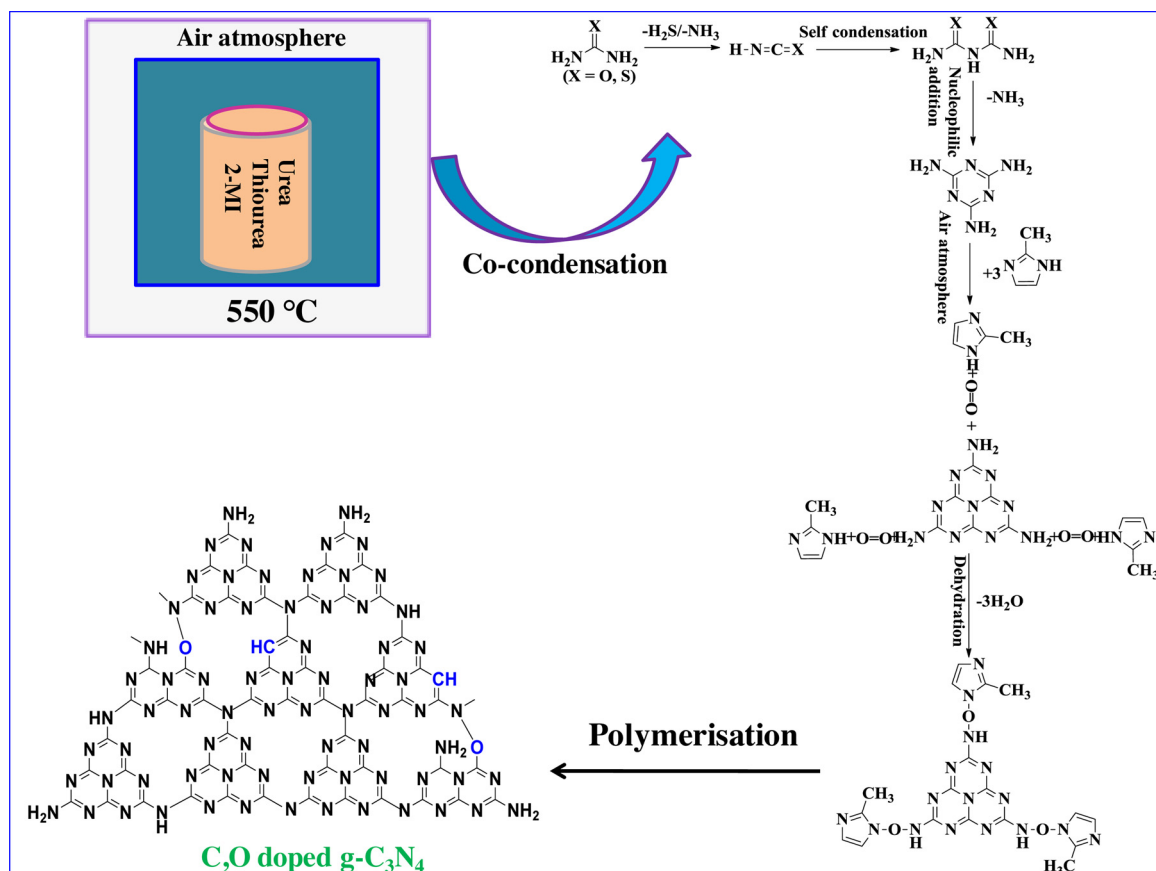
2. Experimental section

Details about the materials, catalyst synthesis and characterization methods, theoretical calculation along with optimized geometries of bulk g-CN and 2-methyl imidazole co-ordinated g-CN (Fig. S1, SI); procedure for photocatalytic CO_2 reduction and H_2O_2 production; photoelectrochemical measurements (PEC); details about the lifetime calculations of the excitons; quantification of H_2O_2 and its limit of detection; oxygen evolution reaction; effect of scavengers in H_2O_2 decomposition; atomic contents of C, N, and O functionalities and their binding energy obtained from the high resolution XPS; optimized geometry for DFT calculations; FE-SEM and EDS of bulk g-CN ; XRD, CO_2 -TPD, XPS, and FE-SEM image of recycled catalyst are provided in the supplementary information (SI) section.

3. Result and discussion

3.1. Physicochemical properties

Bulk graphitic carbon nitride (hereafter represented as g-CN) was synthesized by thermal combustion method using an equal amount (W/W) of urea and thiourea. Surface modification of bulk g-CN was carried out by taking the optimum weight of 2-methyl imidazole (2-MI) together with urea and thiourea (hereafter represented as g-CN-MI-X , $\text{X} = 30, 40, 50$ for 30 mg, 40 mg, and 50 mg of 2-MI, respectively). The co-condensation process was carried out in air which is responsible for the introduction of C and O functionalities in the bulk g-CN [32]. The process of oxygen incorporation was favoured and modulated by 2-MI. Furthermore, to verify the influence of the effects of thermal combustion environment on the material synthesis, 10 g of pure 2-methyl imidazole was calcined in an air atmosphere at 550°C for 4 h. After the heat treatment, 58 mg of black powder residue was obtained. When the synthesis of g-CN was conducted with 2-MI in the inert atmosphere (Argon atmosphere) 682 mg yield of the product was obtained from (5 g urea + 5 g thiourea + 40 mg 2-MI). When a similar experiment was performed in the air atmosphere the yield of the product was 1.784 g. Moreover, a difference in the colour was observed for both the products (material synthesized in argon was pale yellow, whereas, it was brown when synthesized in oxygen atmosphere) (Fig. S2a, SI). These experiments suggest that 2-MI is coordinated with the melem framework and this coordination is facilitated in the oxygen atmosphere. The oxidation of 2-MI was suppressed by the melem framework and its coordination with melem framework was favoured by the air atmosphere. The possible coordination of 2-MI with melem framework for the synthesis C, O co-doped g-CN in the air atmosphere is provided in Scheme 1 which was not facilitated in the Ar atmosphere. Powder X-ray diffraction (PXRD) analysis of 2-MI modified $\text{g-C}_3\text{N}_4$ and the parent $\text{g-C}_3\text{N}_4$ exhibit no-distinction in their powder XRD reflections indicating that incorporation of 2-MI did not affect the basic aromatic motif of $\text{g-C}_3\text{N}_4$



Scheme 1. The tentative formation mechanism for the C, O co-doped polymeric g-C₃N₄ from urea, thiourea and 2-methyl imidazole.

(Fig. 1a). All the materials exhibit a sharp reflection at 27.4° and a weak reflection at 12.6° which can be indexed to 002 and 100 planes, respectively, of standard g-C₃N₄ (Fig. 1a) [48]. Moreover, the variation in 2-MI contents did not disturb the XRD patterns of the other materials synthesized by the co-condensation process. N₂-sorption measurements were carried out to determine the physical characteristics of the materials (Fig. 1b). Almost a flat adsorption is observed for g-C₃N₄. With the increase in 2-MI content, the adsorption above P/P₀ = 0.9 is increased (Fig. 1b). Among all the synthesized photocatalyst, g-CN-MI-40 exhibits the highest BET surface area (60.6 m²/g) indicating that 40 mg of 2-MI (for 5 g of urea and 5 g of thiourea) was the optimum amount for surface modification of parent g-C₃N₄ materials (Table 1). Textural properties of the synthesized materials are provided in Table 1. In order to investigate the influence of 2-MI modification, FTIR, solid-state/liquid state NMR and in-depth XPS analysis were carried out. FTIR spectra of these materials exhibit a sharp band at 807 cm⁻¹ and an envelope of bands in the range of 1200–1600 cm⁻¹ which can be assigned to the bending and stretching vibration modes of aromatic C–N heterocycles (Fig. 1c) [49]. A broadband can be found in the range of 3000–3500 cm⁻¹ which is attributed to the (N–H) or (O–H) vibrations mode, originating from the surface uncondensed amine groups or the absorbed water species (Fig. 1c) [49]. Further, a distinct peak at 1506 cm⁻¹ due to the ‘C = C’ functionality is obtained for all the 2-MI modified g-C₃N₄ materials which are absent in the parent g-C₃N₄ (Fig. 1c) [50]. This further evidences the incorporation of new carbon moiety in g-C₃N₄ framework during the synthesis via co-condensation of urea and thiourea with 2-MI by replacing some of the SP² hybridized nitrogen atoms from the melem framework. To get more insight about 2-MI incorporation, ¹H and ¹³C solid-state NMR of parent g-CN and g-CN-MI-40 samples were recorded (Fig. 1e–f). Sharp signals in the ¹H spectrum appear at 2.7, 5.0, 5.7, and 10.9 ppm for g-CN (Fig. 1e). However, it became broad and more intense in the case of g-CN-MI-40

(Fig. 1e). The less distinguishable peak at 3.0 ppm appears for g-CN-MI-40 which overlaps with peak appeared at 2.7 ppm for g-CN (Fig. 1e). In the case of ¹³C NMR spectrum, two strong ¹³C peaks at 165.6 ppm and 158.0 ppm confirm the chemical shifts due to the presence of C atoms attached to [CN₂(NHx)] and (CN₃), respectively, of a poly(tri-s-triazine) structure (Fig. 1f) [51,52]. An envelope of weak NMR signals in the range of 18–50 ppm for g-CN-MI-40 is due to the incorporation of 2-MI in the CN framework. The ¹³C signals for 2-MI moiety were expected to appear at 13.8, 121.3, and 144.8 ppm, respectively. None of these signals are present in the g-CN-MI-40 confirming that 2-MI was not incorporated in the native form in the sample. During the heat treatment process, 2-MI could break into N₂ and alkene compounds. These alkene compounds could react with C=O, C=C species present in g-CN-MI-40 by Diels-Alder reaction under the thermal condition and form cycloalkane species. The weak ¹³C signals in the range of 18–50 ppm correspond to such cycloalkane and –CH₂–CH₃ species present in the g-CN-MI-40. The ¹³C NMR of the g-CN and g-CN-MI-40 were also measured in the liquid-state. In g-CN, 10 peaks were observed in the ¹³C NMR spectrum whereas, in g-CN-MI-40, 11 peaks were observed in the ¹³C NMR spectrum (Fig. S3a, SI). It may be noted that g-CN and g-CN-MI-40 samples were not soluble in any of the organic solvents, therefore, it was digested in the highly concentrated aqueous H₂SO₄ solution (Fig. S2b, SI). During the H₂SO₄ treatment at 80 °C, the structure of the framework collapsed, therefore, the number of carbon species present in solution NMR was more than the solid-state NMR. Additional peaks present in solid-state and liquid-state NMR confirmed the incorporation of carbon species (through 2-MI in the framework) which is also consistent with the TGA results. In the ¹H NMR spectra, two peaks located at ~10–11 ppm (amino) and 2.5–3.5 ppm (residual water) were observed in both the samples (Fig. S3b, SI). The ¹H NMR signal at ~5–6 ppm could be due to the alkene species present in the g-CN framework (Fig. S3b, SI). An additional strong peak in g-CN-MI-40 is due to the

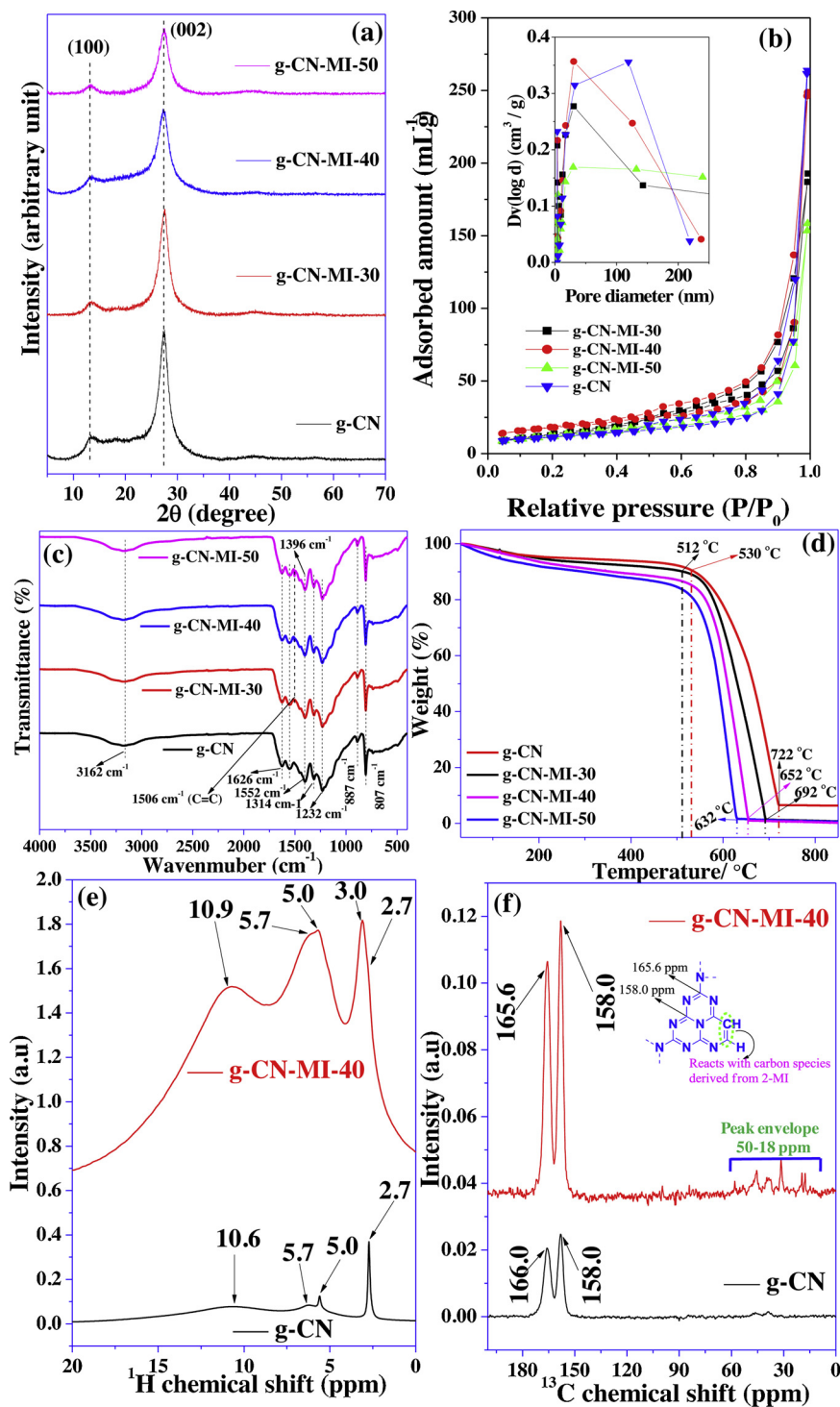


Fig. 1. (a) Powder XRD patterns, (b) N_2 -sorption isotherms, (c) FTIR spectra, (d) TGA profiles of all the materials; (e) 1H and (f) ^{13}C CP-MAS NMR of g-CN and g-CN-MI-40.

Table 1

Physicochemical properties of all the synthesized materials.

| Sample | Surface area, S_{BET} (m^2/g) | Total pore volume (cc/g) | CO_2 adsorption at $(P/P_0) = 1$ (mmol/g) | Charge transfer resistance R_{ct} (Ω) | Solution resistance R_s (Ω) |
|------------|-------------------------------------|--------------------------|---|--|--|
| g-CN | 39.8 | 0.409 | 0.37 | 6.7 | 29.8 |
| g-CN-MI-30 | 51.8 | 0.298 | 0.49 | 6.3 | 26.8 |
| g-CN-MI-40 | 60.6 | 0.386 | 0.69 | 7.1 | 21.5 |
| g-CN-MI-50 | 41.5 | 0.245 | 0.44 | 5.9 | 28.4 |

hydrogen atoms attached to the carbon species incorporated after the addition of 2-MI, as confirmed from ^{13}C NMR discussed above. Thermogravimetric analysis results indicate that g-CN has higher thermal stability than all the 2-MI modified g-CN materials (Fig. 1d). The TGA analysis confirmed that the thermal stability of 2-MI itself was very low and its decomposition took place in the temperature range of 108–178 °C (Fig. S4, SI). However, bulk g-CN starts decomposition at 530 °C whereas all g-CN-MI materials exhibit lesser decomposition temperature of 512 °C. Again, all the g-CN-MI samples have 100% weight loss, but at the same measurement condition, complete decomposition did not take place for pristine g-CN reflecting its higher thermal stability (Fig. 1d). Moreover, the complete decomposition temperature for different MI modified samples also varied which indicate that different contents of C and O were co-doped by replacing some of the N atoms into the melem framework of g-CN during the co-condensation process (Fig. 1d). The lesser thermal stability of the g-CN-MI samples is due to the lower thermal stability of 2-MI and incorporation of new carbon and oxygen functionalities which easily decomposed the C and O in the form of CO_2 and H_2O from the resulting material during the TGA measurement. This result is also consistent with the CO_2 -TPD analysis which will be discussed later.

Micro-structure morphological information was obtained from the FE-SEM analysis for parent g-CN and g-CN-MI-40. Urea/thiourea derived g-CN exhibits a porous architecture which closely resembles sponge-like morphology (Fig. 2a-b and Fig. S5c, SI). FE-SEM images recorded for g-CN-MI-40 shows that some morphological changes are observed after 2-MI incorporation during the synthesis (Fig. 2c-d). g-CN-MI-40 exhibits two domains, floppy cotton-like domain and a domain containing sponge-like structure (Fig. 2c). Some probable domains are observed in g-CN-MI-40 which could be due to the incorporation of the new carbon and oxygen functionalities provided by 2-MI in g-CN-MI-40 (Fig. 2d). The FE-SEM images exhibit very similar morphological information for g-CN-MI-30 (Fig. S5a, SI), and g-CNMI-50, respectively (Fig. S5b, SI). Interestingly, the comparative EDS analysis obtained for g-CN-MI-40 (Fig. 2e-f) and g-CN (Fig. S5d-f, SI) also indicates that oxygen content was higher for the former than the later which is also consistent with the TGA analysis. Atomic force microscopy (AFM) was used to reveal further morphological information for g-CN and g-CN-MI-40 (Fig. 2g-h). AFM image of bulk g-CN indicates the hollow tubular like pattern (Fig. 2g) while g-CN-MI-40 exhibits inter-connected paddy cotton-like morphology (Fig. 2h). TEM analysis further resembles the observation obtained from FE-SEM analysis (Fig. 3, and Fig. S6, SI). Highly cross-linked wrinkle like pattern is obtained for g-CN in its TEM analysis (Fig. S6a-c, SI). The presence of C, N, and O is also confirmed from STEM, HAADF, corresponding elemental mapping and EDAX mapping (Fig. S6d-g, SI). The TEM image of g-CN-MI-40 also has probable domains very similar to that it was observed in its FE-SEM investigation (Fig. 3a-c). TEM images of different magnification for g-CN-MI-40 are presented along with HAADF images, elemental mapping of domains corresponding to various elements, and EDAX mapping present in the sample (Fig. 3d-g). The TEM image of g-CN-MI-40 exhibits the nanostructure very similar to the TEM images of parent g-CN which exhibits highly crossed-linked wrinkle shape nanostructure (Fig. S6, SI).

The surface chemical composition of g-CN and g-CN-MI-40 was confirmed from the surface survey & high-resolution X-ray photoelectron spectroscopic analysis (Fig. 4). The surface survey XPS confirms the presence of C, N, O elements in g-CN and g-CN-MI-40 materials (Fig. 4a). A close inspection of the surface survey spectrum clearly indicates that the signal intensities corresponding to O 1s are comparatively higher for g-CN-MI-40 than the bulk g-CN (Fig. 4a) while the N 1s signal of g-CN-MI-40 is diminished than the signal intensity of N 1s in the bulk g-CN. Although the surface survey XPS implies that the C 1s signal

the intensity remains slightly higher in g-CN even after the surface modification in g-CN with 2-MI (g-CN-MI-40) but the atomic % contents

of C 1s acquired from the surface survey analysis confirms the presence of a higher amount of carbon in g-CN-MI-40 (Fig. 4a-b and Table 2). This result further confirms that some of the SP^2 -(N) atoms were replaced by the newly introduced carbon atoms provided by 2-MI during the synthesis (Table 2) [44]. Notably, the atomic contents (%) of C, N, and O retrieved from the surface survey XPS analysis further confirms the presence of higher amount of C and O while lower amount of N in g-CN-MI-40 (Fig. 4b and Table 2). This validates the earlier discussion about the replacement of N during the air induced synthesis which facilitated the incorporation of new oxygen and carbon functionalities in g-CN-MI-40 by reacting (urea + thiourea) with 2-MI which is also in accordance with the NMR analysis.

The de-convoluted high-resolution C 1s spectrum of g-CN indicated the presence of three types of carbon species at the binding energy of 284.8 eV, 286.3 eV, and 288.3 eV, respectively, which can be assigned to the adventitious type carbons (SP^3 , C–C) and carbon attached to nitrogen as (C–NH) and (N=C–N) of the CN units, respectively, of the melem framework with separate arrangement (Fig. 4c) [32,44]. The peak areas corresponding to these different functionalities are provided in Table S1 in which the highest peak area was acquired by the (N=C–N) carbon of melem framework. However, in the high resolution C 1s spectra of g-CN-MI-40, four different types of carbon species were obtained at the binding energy of 284.8 eV, 287 eV, 288.1 eV, and 288.6 eV, respectively, which could be ascribed to the (SP^3 , C–C), (C–NH), (N=C–N) and (N–C–O/C–O) carbons, respectively [32,41,44,46]. The appearance of one extra peak at 288.6 eV corresponding to (N–C–O) bonding confirms the incorporation of a new type of carbon species due to the surface modification by 2-MI [32]. The peak areas and atomic % of different carbon functionalities for g-CN and g-CN-MI-40 are provided in Table S1.

Again, in the high-resolution N 1s spectrum of g-CN, the peak corresponding to 398.8 eV, 400.3 eV, and 401.4 eV can be assigned to the tertiary nitrogen (N-(C)₃), sp^2 -hybridized nitrogen in triazine rings (C–N=C), and the surface amino groups (C–NH₂) moiety in the CN framework, respectively (Fig. 4d) [32,41–47]. However, in the high-resolution spectra of N 1s in g-CN-MI-40, all these three peaks correspond to the (N-(C)₃), (C–N=C), and (C–NH₂) are shifted to lower binding energy at 398.7 eV, 399.4 eV, and 401 eV, respectively, (Fig. 4d) which indicates that 2-MI modification leading to the alteration of surrounding chemical environments of N 1s in g-CN-MI and also due to the introduction of more oxygen atoms in the CN framework having higher electronegativity (E.N: O~3.5, N~3.0, C~2.5) [32]. The different nitrogen functional contributions and peaks areas in g-CN and g-CN-MI-40 are provided in Table S1, SI.

The Surface survey spectra of g-CN and g-CN-MI-40 confirm that upon 2-MI addition, the resultant material exhibited a higher concentration of surface oxygen species (Fig. 4b). In the high resolution O 1s spectrum of g-CN, two peaks at the binding energy of 532.3 eV and 533.5 eV are originated due to the surface hydroxyl groups (O–H) and the (O–N) intermediates which would have resulted from the intermediates during the thermal induced polymerization of urea and thiourea (Fig. 4e) [32]. Interestingly, in the high-resolution spectrum of g-CN-MI-40, three peaks at the binding energy of 531.1 eV, 532.2 eV and 533.4 are assigned to the (N–C–O), hydroxyl groups (O–H) and the (O–N) oxygen (Fig. 4e). Here also the high electronegativity of oxygen and incorporation of new oxygen resulted in the lowering in the binding energies of the (O–H) and (N–O) functionalities in g-CN-MI-40 (Fig. 4e) [32,42–45]. The appearance of a new peak at 531.1 eV in the O 1s spectrum of g-CN-MI-40 is indicative of the presence of (C–O) and/or (C–N–O) bonding environments confirming the introduction of new oxygen in g-CN-MI-40 (Fig. 4e) [32,52–55]. The different oxygen functionalities and their corresponding peaks area in g-CN and g-CN-MI-40 are provided in Table S1, SI. So, the detailed XPS measurement confirms the co-doping of carbon and oxygen by replacing some of the nitrogen from the melem frameworks in g-CN-MI-40 during the air induced thermal polymerization between (urea + thiourea) and 2-MI.

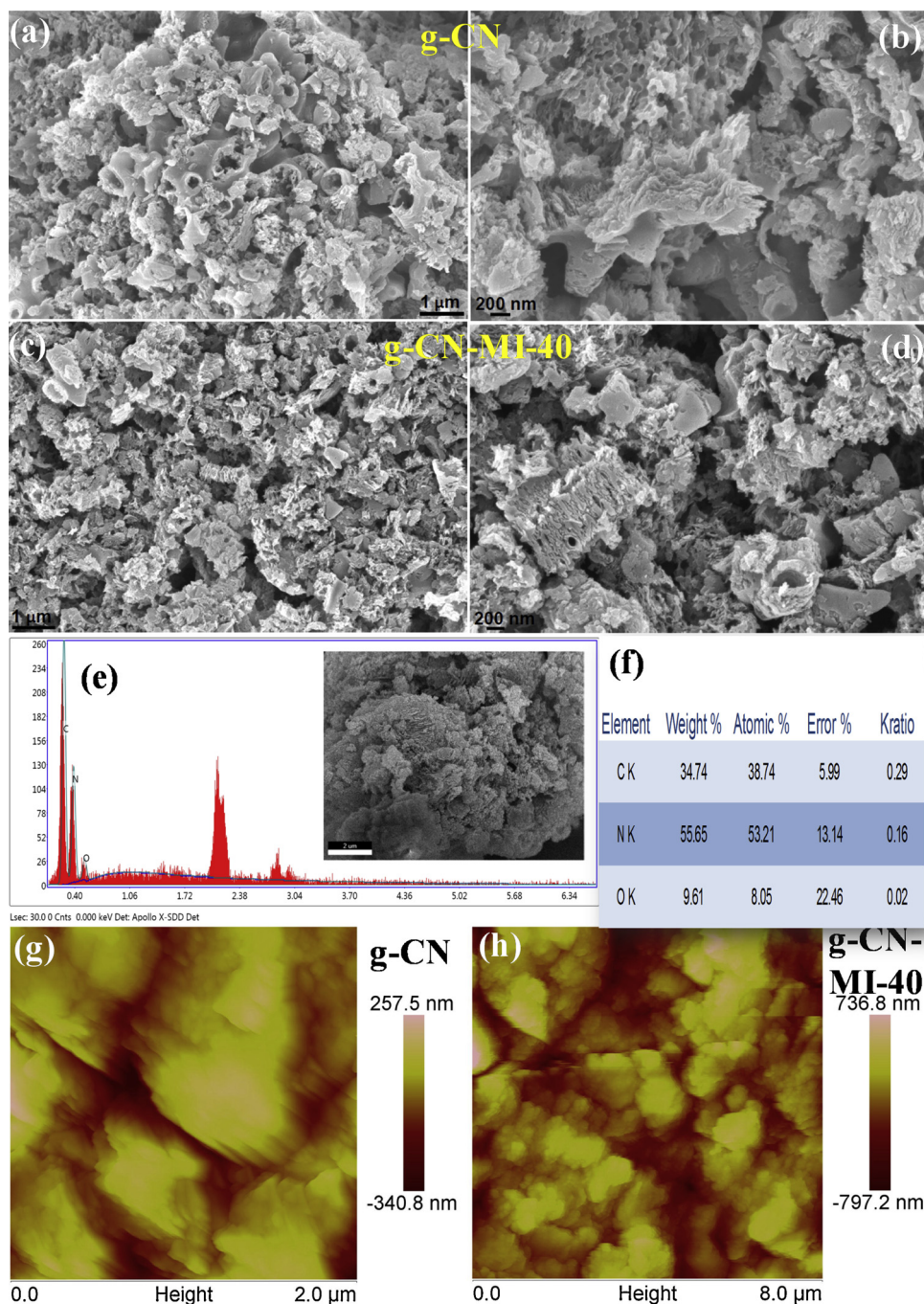


Fig. 2. FE-SEM images of (a–b) g-CN; (c–d) g-CN-MI-40; (e–f) EDS and elemental contents of g-CN-MI-40; AFM images of (g) g-CN and (h) g-CN-MI-40.

The contents of O, C, N retrieved from XPS analysis for g-CN and g-CN-MI-40 are provided in Table 2 and Fig. 4b for g-CN and g-CN-MI-40 which implies that O and C contents are enhanced to 79% and 5.1%, respectively, in terms of atomic percentage. These observations are also in line with the EDS analysis of g-CN and g-CN-MI-40.

Elemental analysis was also carried out to confirm the doing impact due to 2-MI modification the increase in the O content due to 2-MI modification. The contents of oxygen in g-CN-MI-40 (36%) was found to be higher than the parent g-CN (32%) (Fig. S7, SI). The obtained results are also in line with XPS and TGA analysis results.

Photophysical properties measured for various samples prepared in this study further confirm the changes observed after the 2-MI incorporation. UV–vis measurements in diffused reflectance (DRS) mode indicate that 2-MI incorporation did not change the feature of the

absorption spectrum, but it only shifted the absorption edge. Photograph of the samples shows that upon 2-MI incorporation, an apparent colour change from yellow (for g-CN) to orange-yellow is observed which is indicative for the shift in the absorption edge (Fig. 5a, Inset). All the g-CN-MI materials show a red-shift absorption in the region of 450–700 nm, whereas, g-CN exhibits adsorption edge in the range of 400–450 nm (Fig. 5a). 2-MI incorporation in g-CN results in a red-shift of the band absorption edge from 460 nm (g-CN)→550 nm (g-CN-MI-30)→585 nm (g-CN-MI-40)→610 nm (g-CN-MI-50) with a tail extend up to 750 nm in the visible-light region which is probably due to the incorporation of new oxygen functionalities (Fig. 5a) [32,42,44,54]. Band-gap values for g-CN, g-CN-MI-30, g-CN-MI-40, and g-CN-MI-50 were determined to be 2.77, 2.67, 2.62, and 2.57 eV, respectively, from the tau plot, using the Kubelka-Munk function, $[(\alpha h\nu)^{1/2} \text{ vs. } h\nu]$

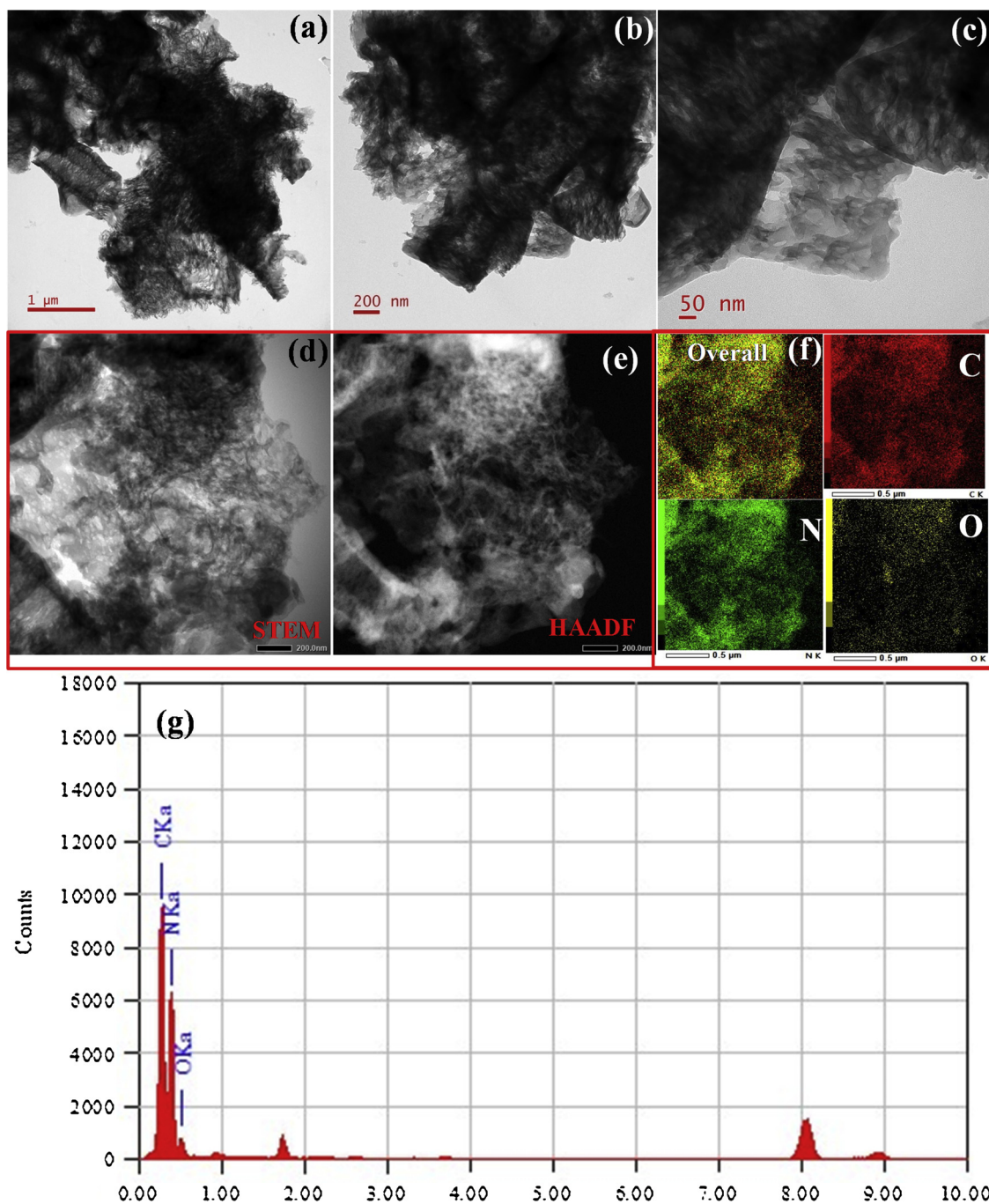


Fig. 3. TEM images of g-CN-MI-40 (a–c), STEM and HAADF (d–e), and corresponding elemental distribution of C, N, O (f), and EDAX (g).

(Fig. 5b) [56]. These measurements confirm that the lowering in band gap is observed after 2-MI modification due to the co-doping impact of carbon and oxygen in the bulk g-CN. The increased photoabsorption of g-CN-MI samples in the visible region (500–750 nm) can be attributed to the multiple reflection/scattering of the incident light within the porous floppy structure. Steady-state photoluminescence (SSPL) study further confirms the decrease in the band gap value in g-CN-MI samples compared to the bulk g-CN. A peak maxima centered at 446 nm in the SSPL is mainly due to the band to band electronic transition (Fig. 5c). Moreover, the significant lower intensity in steady-state PL emission of CN-MI-40 confirms the lower probability of the band-to-band electrons-hole recombination (Fig. 5c) [56]. Time-resolved PL spectra recorded for g-CN, CN-MI-30, g-CN-MI-40, and g-CN-MI-50 are presented in Fig. 5d. A tri-exponential fitting method was employed to obtain the

average lifetimes and percentage contributions in the excited states (see supporting information (SI) for more details) [57]. Shorter lifetime (τ_1) and longer lifetime (τ_2) of g-CN-MI samples are decreased with increase in 2-MI incorporation when compared to bulk g-CN. This result led to the lowering of the average lifetime of g-CN-MI samples compared to bulk g-CN. The average lifetime for g-CN, CN-MI-30, CN-MI-40, and g-CN-MI-50 are calculated to be 7.08 ns, 6.95 ns, 5.59 ns, and 6.35 ns, respectively (Table 3). The decrease in average lifetime indicates the efficient non-radiative transfer of photogenerated charge carriers in g-CN-MI-40 due to the shorter distance need to be covered/fast transportation towards the reactants by the excitons and better charge transfer pathways produced by 2-MI incorporated modified samples than the bulk g-CN [34]. The highest rate of electron ejection efficiency is obtained for g-CN-MI-40 ($k_{e_{inj}} = 0.18 \text{ (ns)}^{-1}$) among the synthesized

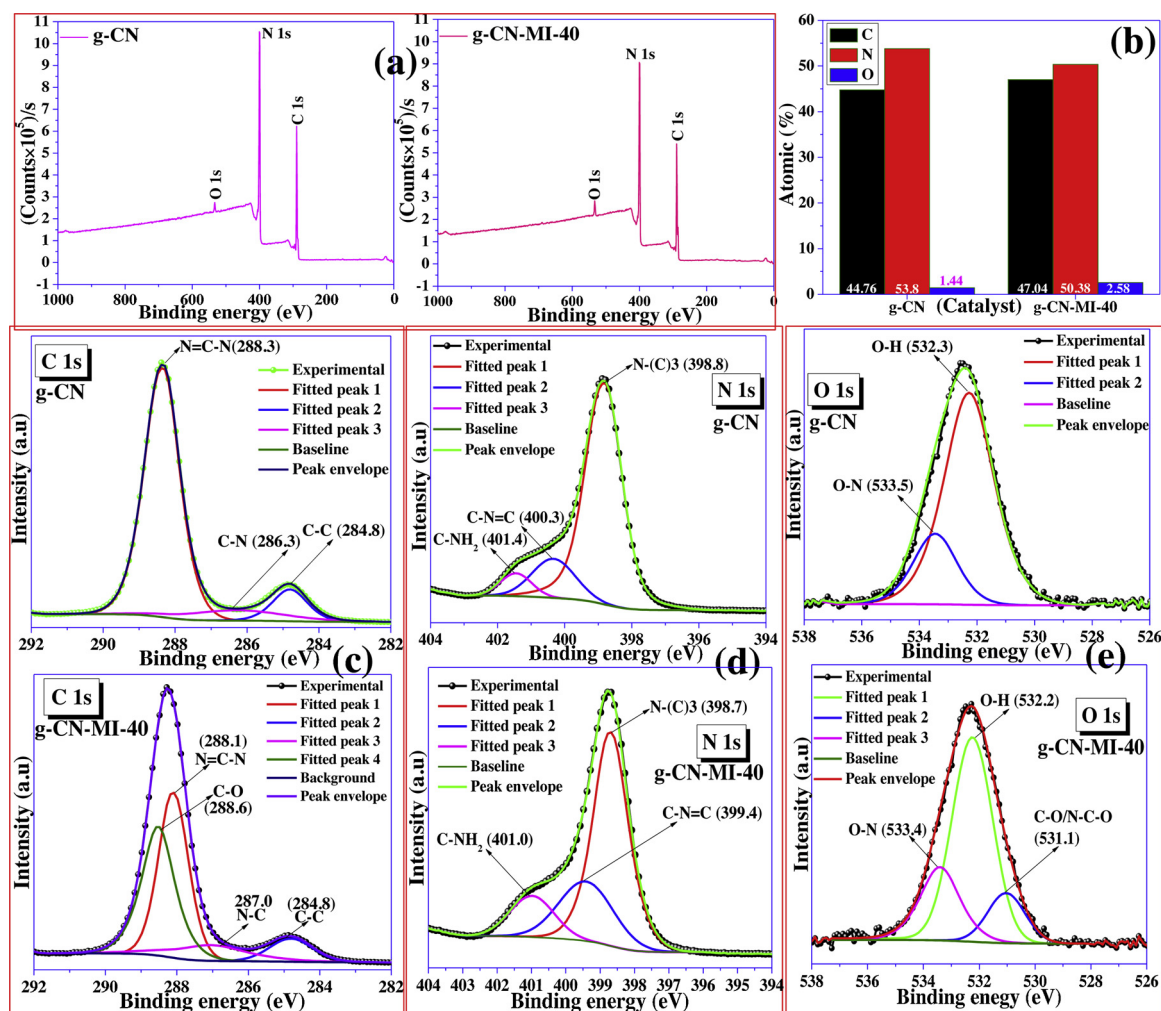


Fig. 4. (a) Full surface survey XPS spectrum; (b) Atomic % contents of C, N and O; High-resolution (c) C1s, (d) N 1s, and (e) O 1s of g-CN and g-CN-MI-40 (The C 1s binding energy at 284.7 eV was used to calibrate the XPS measurements).

g-CN-MI photocatalysts which imply that it might exhibit better photocatalytic activity (Table 3).

3.2. Evaluation of the photocatalytic activity

3.2.1. CO₂ uptake and CO₂-TPD

The CO₂ photoreduction on any catalyst solely depends upon its effective CO₂ adsorption over the catalyst surface [58]. Therefore, CO₂ uptake measurements of all the catalysts were analyzed from the CO₂ adsorption isotherm measured at 294 K. As shown in Fig. 6a, the CO₂ uptake capacities of all the 2-MI modified g-CN are better than bulk g-CN which is more prominent at the higher P/P₀ region. Among all the

investigated materials, at [P/P₀ = 1], bulk g-CN exhibits the lowest CO₂ uptake of 0.37 mmol/g, whereas, g-CN-MI-40 adsorbs the highest amount of CO₂ of 0.69 mmol/g, which is almost twice to that of bulk g-CN (Fig. 6a). The CO₂ uptake amount of other materials is provided in Table 1. The difference in the CO₂ uptake capacities of bulk g-CN and 2-MI modified g-CN materials can also be justified from the CO₂-TPD profiles (Fig. 6b). The lower amount of CO₂ is desorbed from the bulk g-CN at around 445 K. With the increase in the 2-MI content, amount of CO₂ desorption is increased, however, with further increase in the 2-MI content, amount of CO₂ desorption is decreased at 420 K (Fig. 6b). The highest amount of CO₂ is desorbed from g-CN-MI-40. Close inspection of CO₂-desorption profile, it can be concluded the CO₂ is desorbed at a

Table 2

Details of elemental analysis retrieved from XPS surface survey analysis for g-CN and g-CN-MI-40 photocatalyst.

| Catalyst | | g-CN | | | | | | | |
|----------|----------|------------|--------|------------|---------------|-----------------|----------|----------|----------|
| Elements | Start BE | Peak BE | End BE | Height CPS | PP Height CPS | Area (P) CPS.eV | Area (N) | Atomic % | PP At. % |
| N 1s | 406.58 | 399.06 | 396.08 | 215150.7 | 221345.52 | 404222.2 | 3650.7 | 53.80 | 48.54 |
| C 1s | 296.18 | 288.56 | 282.78 | 131030.16 | 134173.46 | 216066.38 | 3037.08 | 44.76 | 45.8 |
| O 1s | 537.38 | 532.66 | 528.78 | 6536.57 | 6689.47 | 16872.86 | 97.94 | 1.44 | 5.66 |
| Catalyst | | g-CN-MI-40 | | | | | | | |
| N 1s | 406.98 | 399.17 | 395.88 | 178303.64 | 185069.17 | 345253.37 | 3118.38 | 50.38 | 46.32 |
| C 1s | 296.08 | 288.67 | 282.98 | 107566.91 | 110278.85 | 207103.46 | 2911.3 | 47.04 | 42.96 |
| O 1s | 537.38 | 532.78 | 527.78 | 10764.64 | 11110.31 | 27549.53 | 159.93 | 2.58 | 10.72 |

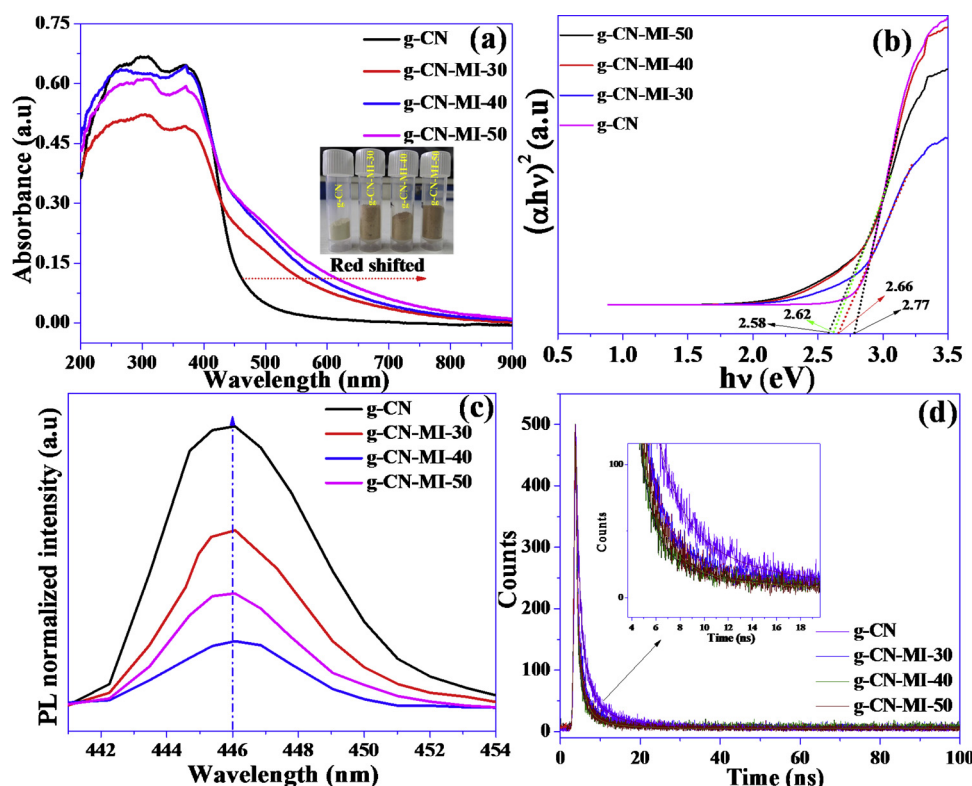


Fig. 5. (a) DRUV-Visible spectrum and (b) Corresponding tau plots of all the photocatalyst, (c) Steady-state photoluminescence spectrum, and (d) Lifetime PL profiles (Inset shows the enlarged area).

Table 3

Lifetime profile and corresponding carrier dynamics information of the synthesized photocatalysts.

| Samples | χ^2 | τ_1 | τ_2 | τ_3 | α_1 | α_2 | α_3 | $\langle \tau \rangle$ ns | K_{inj} (ns^{-1}) |
|------------|----------|----------|----------|----------|------------|------------|------------|---------------------------|---------------------------------------|
| g-CN | 1.084 | 0.579 | 2.132 | 8.602 | 21.88 | 39.69 | 38.44 | 7.08 | 0.14 |
| g-CN-MI-30 | 1.194 | 0.240 | 1.595 | 8.402 | 28.44 | 40.77 | 30.80 | 6.95 | 0.15 |
| g-CN-MI-40 | 1.216 | 0.211 | 1.367 | 7.278 | 39.20 | 39.21 | 21.61 | 5.59 | 0.18 |
| g-CN-MI-50 | 1.163 | 0.225 | 1.256 | 8.070 | 36.62 | 32.17 | 18.56 | 6.35 | 0.16 |

relatively lower temperature for 2-MI modified samples than bulk g-CN (Fig. 6b) which is due to the introduction of new oxygen functionalities. This result is consistent with the CO_2 uptake capacities of all the synthesized materials. 2-MI modification leads to the incorporation of new carbon and oxygen functionalities resulting in the higher CO_2 uptake and higher amount of CO_2 desorption. The heat of adsorption energies (λ) for CO_2 over pristine g-CN and g-CN-MI-40 are calculated to be 10.3 and 7.85 kJ/mol, respectively. The lowering in the heat of adsorption further indicates that the incorporation of the optimum amount of 2-MI in bulk g-CN surface facilitates the CO_2 adsorption which is expected to facilitate the catalytic reduction over its surface. This experimental finding for CO_2 adsorption over the photocatalyst is also supported by the density functional theory, and the results are discussed below.

3.2.2. Theoretical calculation of CO_2 binding energy

DFT calculation was used to compare the adsorption energies of CO_2 on the g- C_3N_4 surface and 2-MI coordinated g- C_3N_4 surface. The optimized geometries for bulk g-CN and MI co-ordinated g-CN are provided in Fig. S1, SI. The first principle DMol³ calculations show a higher interaction with adsorbed CO_2 over 2-MI coordinated g- C_3N_4 surface with adsorption energy -0.133 eV (-12.86 kJ/mol) as compared to the g- C_3N_4 surface having relatively lower adsorption with the adsorption energy of -0.127 eV (-12.39 kJ/mol) (Fig. 7a-b). The 2-MI coordinated g- C_3N_4 surface has a higher affinity for CO_2 adsorption, resulting in a better photocatalytic CO_2 reduction. The results are further confirmed by CO_2

uptake experiments (Fig. 6a). The total density of states (TDOS) of 2-MI coordinated g- C_3N_4 show slight shift in conduction band position (0.25 eV) towards the CO_2 reduction potential as compared to g- C_3N_4 (0.42 eV) indicating faster CO_2 molecule activation over the 2-MI coordinated g- C_3N_4 surface (Fig. 7c). This can be further justified as: the reduction potential of CO_2 to CH_3OH is -0.38 eV. The advantage of the system with the potential closer to the thermodynamic potential (-0.38 V) is that it can theoretically use longer wavelengths of light to effect carbon dioxide reduction [59]. The electron transfer is faster for the catalyst with conduction band more nearer to the reduction potential of CO_2 under visible light. The 2-MI coordinated g- C_3N_4 (g-CN-MI-40) showed conduction band positioning at 0.25 eV which is lower than conduction band positioning (0.42 eV) of g-CN. This indicates that the 2-MI coordinated g- C_3N_4 allowed faster electron transfer under visible light from the conduction band to reactive sites resulting in faster CO_2 molecule activation than g- C_3N_4 . The energy band structure of pure g- C_3N_4 shows the indirect band gap value of 1.23 eV which is 1.45 eV smaller than the experimental value due to the well-known limitation in DFT [60]. Therefore the experimental results are consistent with the theoretical calculations. In order to measure the impact of C and O co-doping in g-CN framework, room temperature electron paramagnetic spectroscopic (EPR) analysis was conducted over g-CN and g-CN-MI-40 under dark condition. Both the materials exhibit a single Lorentzian peak located at around $G = 3515$ corresponding to the g value of 2.0034 (Fig. 7d) [61]. Apparently, g-CN-MI-40 produces a

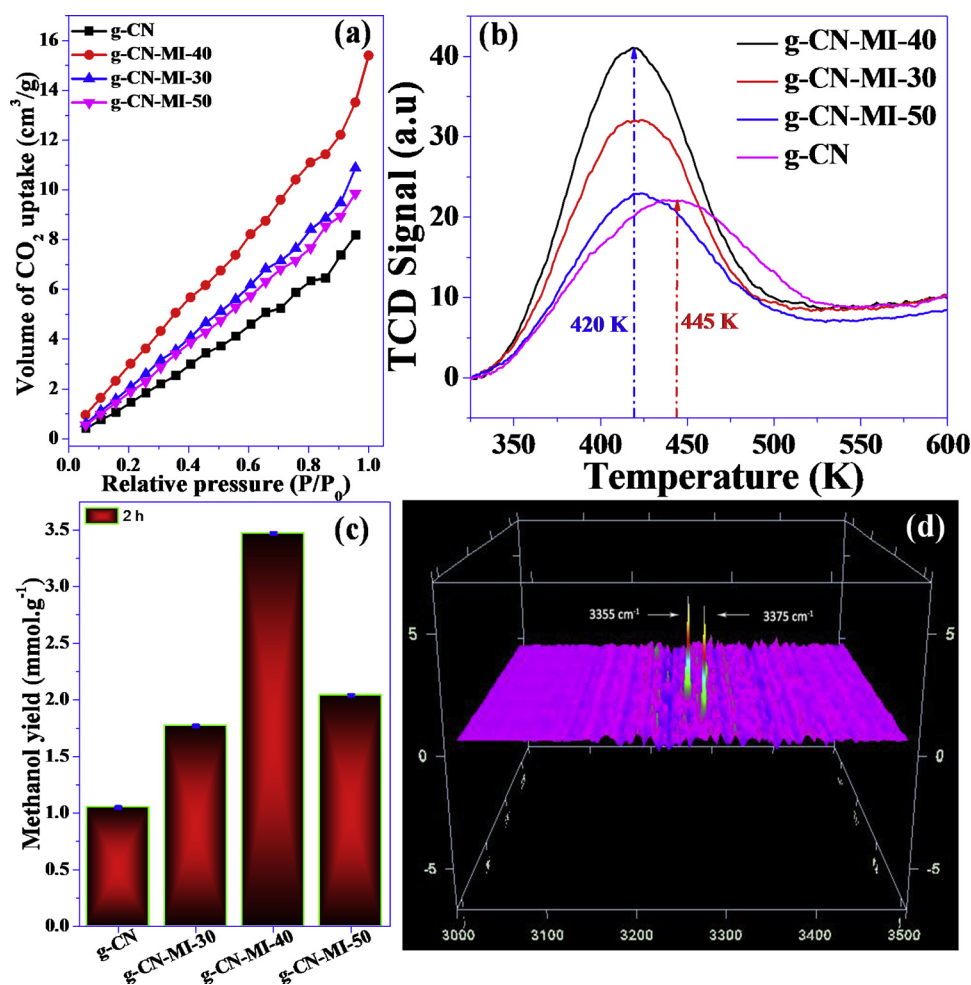


Fig. 6. (a) CO₂-adsorption isotherms, (b) CO₂-TPD profiles, (c) Methanol yield after 2 h for all the catalysts (errors bar represent $n = 3$ and ± 0.1), and (d) Mid-region in-situ FTIR spectrum recorded after 6 h of reaction for the CO₂ photoreduction reaction over g-CN-MI-40.

more intense signal which indicates that the number of unpaired electrons is higher in g-CN-MI-40 than g-CN which is provided by the co-doped O and C present in g-CN-MI-40. Therefore, g-CN-MI-40 can effectively donate these electrons to the antibonding 'C = O' orbital of CO₂ and enforce it to adopt more bending geometry from the linear one [24]. This facilitates the CO₂ binding and reduction reaction over 2-MI modified g-CN catalysts.

3.2.3. Visible light assisted CO₂ photoreduction

Control experiments and reaction parameters were optimized for CO₂ photoreduction before detailed investigation. In the absence of CO₂ gas or in the presence of inert gas N₂, no product was obtained even after a prolonged reaction time (Table 4).

In this reaction 10 ml tri-ethanol amine (TEOA) was used as a sacrificial electron donor. The reaction was further performed with TEOA alone which did not produce any CH₃OH as a product. This confirmed that CO₂ is the sole carbon source for hydrocarbon fuel production. Several CO₂ photoreduction reactions conducted over g-C₃N₄ as a photocatalyst with and without ¹³C isotope tracing experiment in the recent past suggest that the adventitious carbon of g-C₃N₄ was not converted to methanol rather the CO₂ gas was the only source for carbon which was converted into various C1-fuels [63–67]. This is further justified in our work by stability analysis of the recovered catalyst which will be discussed in the recyclability study section. Moreover, in the absence of light, the reaction did not proceed indicating the reaction is dominated by visible light (Table 4). Control experiments further indicate that 100 mg catalyst and 50 ml H₂O solution

(H₂O:TEOA = 40:10 V/V) was found to be the best for obtaining the highest yield of CH₃OH. After 2 h of reaction, the methanol yields over g-CN, g-CN-MI-30, g-CN-MI-40, g-CN-MI-50 were found to be 1.05, 1.71, 3.47, and 2.06 mmol/g, respectively (Fig. 6c). The catalytic data shows that the methanol yield from the CO₂ reduction reaction is almost twice for g-CN-MI-40 than bulk g-CN. The catalytic activity of g-CN-MI-40 is also found to be better than several g-C₃N₄ based catalysts reported in the literature (Table S2, SI) [22,23,30,32,33,61,62,68–70]. More importantly, in the present photocatalytic reaction, the selective production of methanol takes place, which is beneficial for sustainable photocatalysis. For comparative purpose, g-C₃N₄ synthesized from different precursors were also investigated under the same experimental setup but the product yield in each case was comparatively lower than the bulk g-CN synthesized from equal content of urea and thiourea. To get a better insight about the reaction mechanism, in-situ Mid-FTIR was performed after 6 h of reaction and obtained FTIR spectrum indicates the presence of two sharp peaks at around 3355 cm⁻¹ (due to the non H-bonded –OH groups of CH₃OH in the vapour phase) and 3375 cm⁻¹ (due to the H-bonded –OH groups of CH₃OH present in the water) which can be ascribed to the –OH stretching frequencies of the generated CH₃OH after the reaction (Fig. 6d) [71]. Again, the GC measurement shows that minute amount of HCHO and HCOOH are formed along with CH₃OH (along with the minute amount of ethanol) which are the active intermediates for this CO₂ reduction (Fig. S8, SI). A peak corresponds to C₂H₅OH in the gas chromatogram indicates the formation possibility of C₂H₅OH as C₂ product over this catalyst [72]. C₂H₅OH is formed possibly due to the dimerization of several C₁

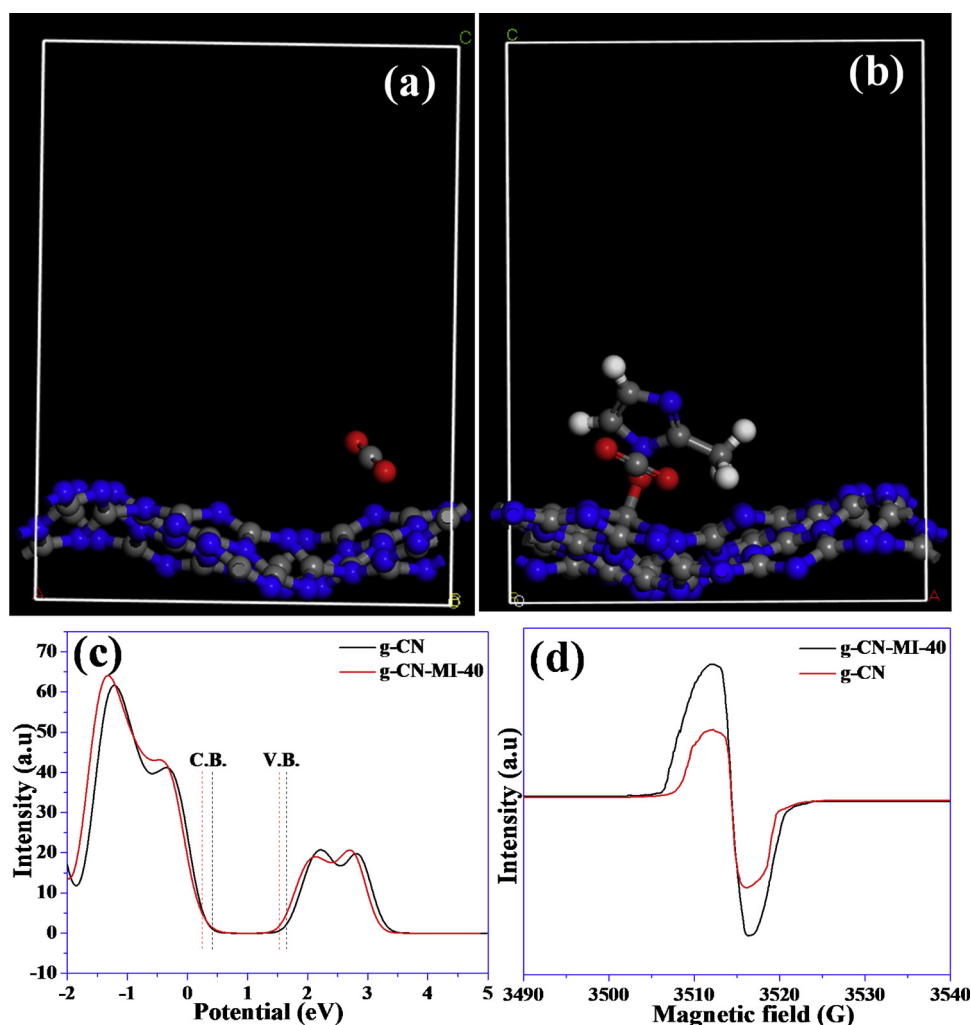


Fig. 7. Optimized geometry of (a) g-CN interacted with CO₂ molecule, (b) g-CN-MI-40 interacted with CO₂ molecule, and (c) Calculated total density of state (TDOS) for g-CN and g-CN-MI-40, and (d) EPR spectra of g-CN and g-CN-MI-40 at ambient temperature under dark condition.

intermediates attached to the surface of the catalyst [32,72]. During the reaction, CO₂ is converted into HCOOH followed by HCHO, which finally produces CH₃OH as the main product. CO₂ photoreduction is a complex reaction because there is a competitive reduction tendency of the light-induced electrons for H⁺ vs. CO₂ which eventually results in the production of H₂ gas which is a back reaction [24,28]. TEOA as a scavenger absorbs the holes from the catalyst surface and the electrons become more reactive which reduce the CO₂ more effectively. Combined in-situ FTIR and GC analysis confirmed the absence of both H₂ and O₂ gas during the reaction and CH₃OH was obtained as a selective

product. After 6 h of reaction, g-CN-MI-40 exhibited 4.18 mmol/g of CH₃OH (Table 4) which indicates the excellent performance of the developed photocatalyst for the CO₂ reduction reaction. The possible mechanism for the CO₂ reduction reaction by the light-induced electrons and holes will be discussed in the next section in this manuscript. The enhancement in the CO₂ reduction performance of g-CN-MI-40 can be attributed to the high CO₂ uptake capacity, lower heat of adsorption energy, and higher surface area compared to the bulk g-CN.

Table 4
Evaluation of photocatalytic CO₂ reduction reaction.

| E.No. | Photocatalyst | Reaction condition ^a | Time (h) | Light Source | Product yield (Methanol/mmol. g ⁻¹) |
|-------|------------------------------|------------------------------------|----------|--------------|---|
| 1. | g-CN | H ₂ O | 4 | Yes | – |
| 2. | g-CN | H ₂ O + N ₂ | 4 | Yes | – |
| 3. | g-CN | H ₂ O + CO ₂ | 6 | No | – |
| 4. | g-CN | H ₂ O + CO ₂ | 6 | yes | 2.8 |
| 5. | g-CN-MI-30 | H ₂ O + CO ₂ | 6 | Yes | 3.70 |
| 6. | g-CN-MI-40 | H ₂ O + CO ₂ | 6 | Yes | 4.18 |
| 7. | g-CN-MI-50 | H ₂ O + CO ₂ | 6 | Yes | 3.91 |
| 8. | g-CN(prepared with melamine) | H ₂ O + CO ₂ | 6 | Yes | 0.11 |
| 9. | g-CN(prepared with urea) | H ₂ O + CO ₂ | 6 | Yes | 1.23 |
| 10. | g-CN(prepared with thiourea) | H ₂ O + CO ₂ | 6 | Yes | 1.02 |

Reaction condition: Reaction performed in suspension system in a custom-made reactor; photocatalyst 100 mg, (H₂O + TEOA = 40 mL + 10 mL), high purity CO₂ gas (99.9%) was used in each case, ^aTEAO, light source 300 W Xenon Lamp, λ = 420 nm, temperature = r.t.

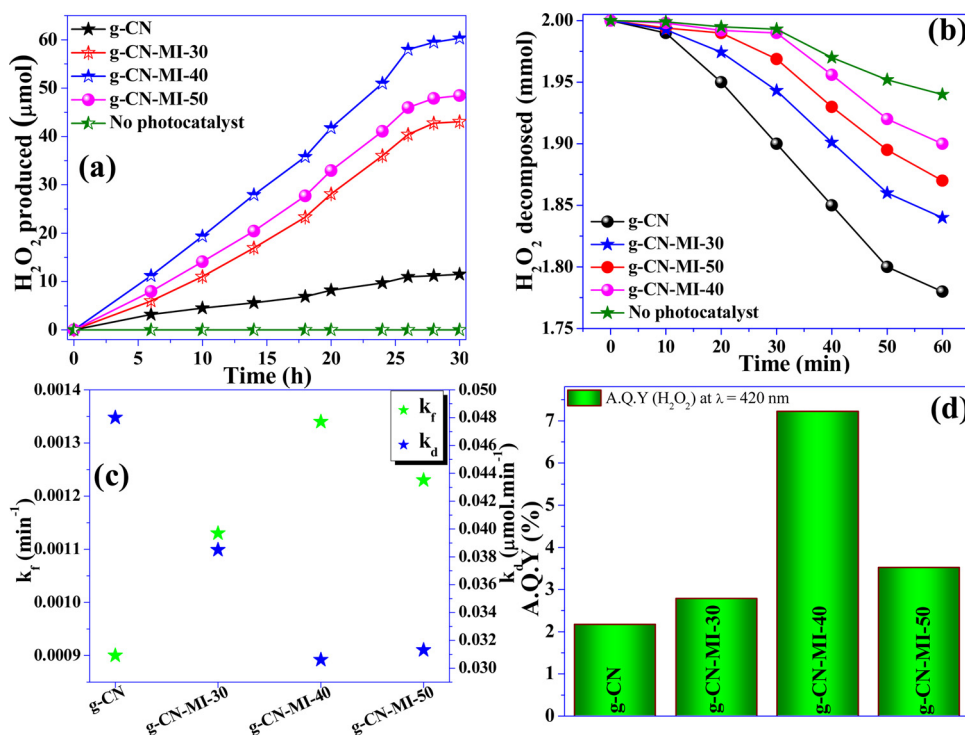


Fig. 8. (a) Photocatalytic H₂O₂ production, (b) H₂O₂ decomposition, (c) Forward and backward rate constant, (d) Apparent quantum yield for H₂O₂ production of all the photocatalysts.

3.3. Visible light assisted H₂O₂ production

The photocatalytic activity of all the synthesized materials for H₂O₂ production under light illumination ($\lambda > 420$ nm) was carried out in O₂ dissolved water without any sacrificial agents and co-catalyst. The catalytic activity data indicate that parent g-CN exhibits very less photocatalytic activity indicating its inferiority for H₂O₂ production (Fig. 8a). The quantity of H₂O₂ produced after 1 h for g-CN-MI-40 (3.2 μmol) is more than three times higher than parent g-CN (0.96 μmol) (Fig. S9, SI). All the 2-MI modified g-C₃N₄ exhibit better catalytic activity than bulk g-C₃N₄ (Fig. 7a). The amount of H₂O₂ production is significantly improved for all the modified g-C₃N₄ photocatalysts which indicate the impact of surface modification of parent g-C₃N₄ with 2-MI. Fig. 8a and Fig. S9, SI further indicates that g-CN-MI-40 produces the highest amount of H₂O₂ among all the employed photocatalysts. A linear increment in the H₂O₂ concentration is observed for all the photocatalysts up to a test run of 24 h, after which its concentration becomes steady indicating that the H₂O₂ decomposition is limiting the H₂O₂ production rate. In the long run of 30 h, g-CN, g-CN-MI-30, g-CN-MI-40, and g-CN-MI-50 photocatalyst produce 11.5, 43.1, 60.3, and 48.3 μmol of H₂O₂, respectively (Fig. 8a). According to the literature reports, H₂O₂ can also decompose to form H₂O and O₂ by the light-induced holes as well as electrons ($\text{H}_2\text{O}_2 + 2\text{h}^+ = 2\text{H}^+ + \text{O}_2$; $\text{H}_2\text{O}_2 + 2\text{e}^- + 2\text{H}^+ = \text{H}_2\text{O} + \text{O}_2$). To understand this phenomenon, control experiments were performed by taking H₂O₂ solution (2 mM), and it was subjected to light illumination with all the photocatalysts. The reaction solution was titrated, and the amount of decomposed H₂O₂ was found to be the highest for parent g-CN (Fig. 8b). Moreover, the lowest quantity of H₂O₂ was decomposed in the presence of g-CN-MI-40 (Fig. 8b). It also suggests that 2-MI incorporation exhibit positive effect for H₂O₂ production since it imparts stability over parent g-C₃N₄ towards H₂O₂ decomposition. This is also well matched with the results observed in the H₂O₂ production for all the photocatalysts. Excess amount of 2-MI (50 mg) blocks the active surface of g-CN which is the reason behind lower H₂O₂ production ability of g-CN-MI-50 than g-CN-MI-40. This investigation further confirms that the optimum amount of

2-MI modification in parent g-CN (g-CN-MI-40) is crucial for obtaining stable photocatalytic material and the highest amount of H₂O₂ in this study. Under visible light irradiation and in the presence of a catalyst, the concentration of H₂O₂ decreased linearly with the reaction time, indicating that the decomposition of H₂O₂ followed zero order kinetics and therefore the rate constant for H₂O₂ decomposition was measured using zero order rate expression (k_d , μmol.min⁻¹) [73]. Similarly, the rate of formation of H₂O₂ followed the first order kinetics because linearity was obtained when $[\ln(\text{concentration}) \text{ vs. time}]$ was plotted, it indicates that the formation of H₂O₂ followed the first order kinetics and therefore the rate constant for the H₂O₂ formation was measured using first order rate expression (k_f , μmol.min⁻¹). The rate constants for light-driven H₂O₂ decomposition and formation were separately evaluated from zero-order and first-order kinetics [73,11]. The calculated k_d and k_f values are presented in Fig. 8c. The k_f value is improved after 2-MI modification over bulk g-CN (0.0009 μmol.min⁻¹) and it becomes the highest for g-CN-MI-40 (0.00134 μmol.min⁻¹). Similarly, the lowest and the highest k_d value are found for g-CN-MI-40 (0.0306 μmol.min⁻¹) and g-CN (0.0480 μmol.min⁻¹) (Fig. 8c). The decomposition of H₂O₂ at higher concentration is mainly caused by the light-induced holes [11,13]. To prove this phenomenon a similar experiment was carried out by taking AgNO₃ and i-PrOH as sacrificial electrons and holes scavengers, respectively. Upon AgNO₃ addition, H₂O₂ decomposition rate was influenced greatly whereas, upon i-PrOH, it did not influence the decomposition rate too much (Fig. S10, SI). These observations further support that valance band holes oxidize the H₂O₂ and facilitate its decomposition under visible light. These results suggest that modification of g-CN with optimum content of 2-MI improves the catalytic activity for H₂O₂ production reaction by imparting extra stability. The apparent quantum yields (A. Q. Y) for g-CN, g-CN-MI-30, g-CN-MI-40, g-CN-MI-50 at 420 nm after 1 h are presented in Fig. 8d. The A. Q. Y is found to be the highest for g-CN-MI-40 (7.23%) which is more than three times higher than the bulk g-CN (2.17%). The influence of reaction environments further indicates that O₂ is the most favourable atmosphere for the light-induced H₂O₂ production for this system. In the N₂ atmosphere, g-CN-MI-40 produced very less amount of H₂O₂

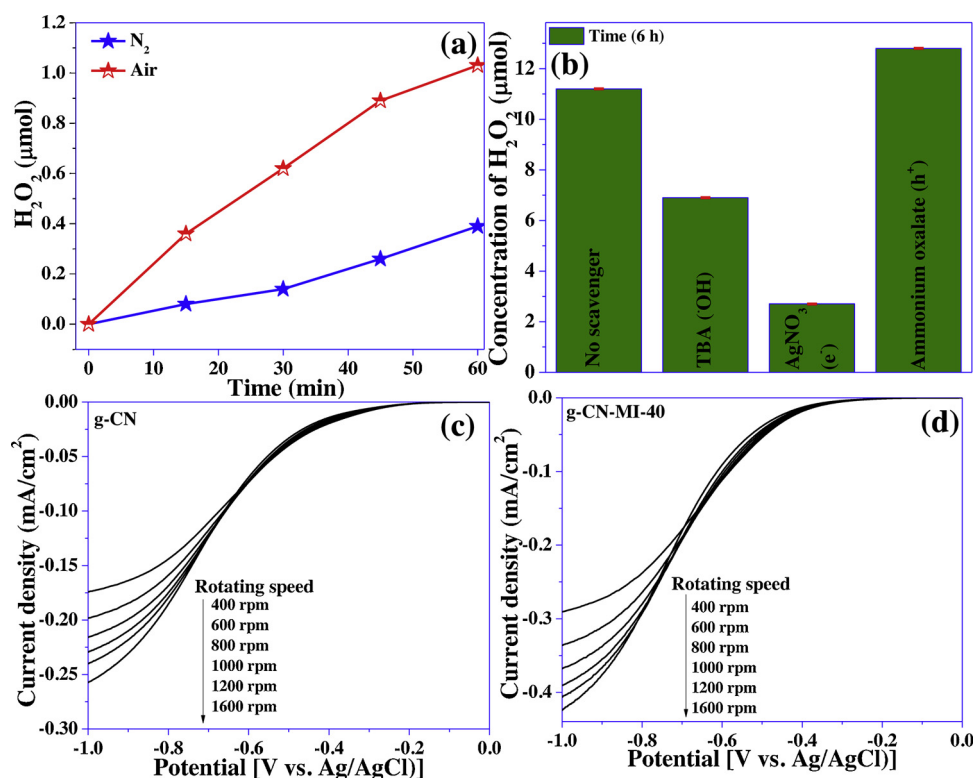


Fig. 9. (a) Effect of reaction environment for H₂O₂ synthesis, and (b) Various scavengers for H₂O₂ production over g-CN-MI-40 photocatalyst (errors bar represent $n = 3$ and ± 0.1), (c-d) LSV profiles obtained from RDE in O₂ saturated 0.5 Na₂SO₄ solutions over g-CN and g-CN-MI-40 under different angular velocities.

(0.39 $\mu\text{mol.h}^{-1}$). But in the presence of air, it produced a comparatively higher amount of H₂O₂ (1.03 $\mu\text{mol.h}^{-1}$) which is due to the presence of O₂ in Air (Fig. 9a). More importantly, in the N₂ atmosphere, the light-induced holes oxidize the water molecules to produce O₂ and H⁺ which in the next step get reduced by the electrons to produce H₂O₂. In case of air, the dissolved O₂ itself is reduced by the light-induced electrons and the present H⁺ leading to the enhanced H₂O₂ production. So based on the observation and the obtained data, it can be concluded that in the presence of O₂ and H₂O the light-induced holes oxidize H₂O to O₂ and H⁺. On the other hand, the bare electrons reduce the O₂ by two electrons to produce O₂²⁻. This finally takes up two protons from the reaction medium to produce H₂O₂ as the final product. Further, to validate this observation, ORR was performed over the catalyst coated electrode using RDE in the O₂ saturated Na₂SO₄ solution (pH = 7). The LSV profiles were obtained by setting the desired potential window under varying rpm using RDE (Fig. 9c-d). The number of electrons involved in the O₂ reduction reaction can be obtained from K-L plot: [15,31]

$$1/j_{\text{lim}} = 1/j_{\text{lev}} + 1/j_k,$$

where, j_{lim} , j_{lev} , and j_k are the limiting current, Levich current, and kinetic current, respectively using the standard parameter (See supporting information, SI, for details).

From the obtained data, the number of electrons (n) for O₂ reduction was found to be 2.46 for bulk g-CN whereas it was 2.24 for g-CN-MI-40 which is close to the theoretical value of $n = 2$ for the two electrons reduction of O₂ to H₂O₂ (Fig. S11, SI) [74]. Higher j_k values obtained for g-CN-MI-40 over bulk g-CN implies its faster kinetics for the O₂ reduction reaction. Since the catalyst can produce H₂O₂ in the N₂ atmosphere also, therefore, it indicates that the catalyst has water oxidation capability. The water oxidation reaction was evaluated with the oxygen evolution reaction in dark condition with the help of LSV. The polarisation profile indicates that g-CN-MI-40 requires an onset potential of 1.69 V with an overpotential of 0.46 V since the standard

water oxidation potential is 1.23 V vs. RHE (Fig. S12, SI) [15]. But the bulk g-CN attains OER at an onset potential 1.76 V vs. RHE which corresponds to the overpotential of 0.53 V vs. RHE (Fig. S12, SI). This finding further indicates that 2-MI modified g-CN-MI-40 has better OER performance than bulk g-CN which leads to its better H₂O₂ production catalytic activity.

3.4. Photoelectrochemical performance and band structure

Ultraviolet photoelectron spectroscopy (UPS) and valance band x-ray photoelectron spectroscopy (VBXPS) are well recognized and precise techniques for the determination of valance band edge of a photocatalyst [32,33]. The UPS and corresponding VBXPS was recorded for bulk g-CN and g-CN-MI-40 and the data are provided in Fig. 10a-b. The VBXPS obtained from the UPS analysis determines the valance band edge potentials for g-CN and g-CN-MI-40 as 1.87 and 1.77 eV, respectively (Fig. 10b). For both the materials, the VBXPS edge is located below the potential of 2.0 eV without any apparent shifting (Fig. 10b). The lowering in the valance band potentials of 0.10 eV caused in the case of g-CN-MI-40 is due to the co-doping effect of carbon and oxygen in the bulk g-CN (Fig. 10b) [32].

Photoelectrochemical (PEC) performances of the materials were evaluated with the help of linear sweep voltammetry (LSV), transient photocurrent ($i-t$) response, Mott-Schottky analysis, and electrochemical impedance spectroscopic (EIS) measurement under dark and light condition. LSV profiles depict that under dark condition, both bulk g-CN and g-CN-MI-40 exhibited almost negligible current which indicates that excitons generation did not take place in the absence of light (Fig. 11a). But in the light illumination, both the catalysts exhibit significant higher current density (about 10 and 14 times higher for g-CN (0.010 mA/cm²) and g-CN-MI-40 (0.016 mA/cm²), respectively than the dark condition (Fig. 11a). This improvement mainly arises because of the light-induced charge carrier's generation. Transient photocurrent response ($i-t$) measurement is another reliable technique

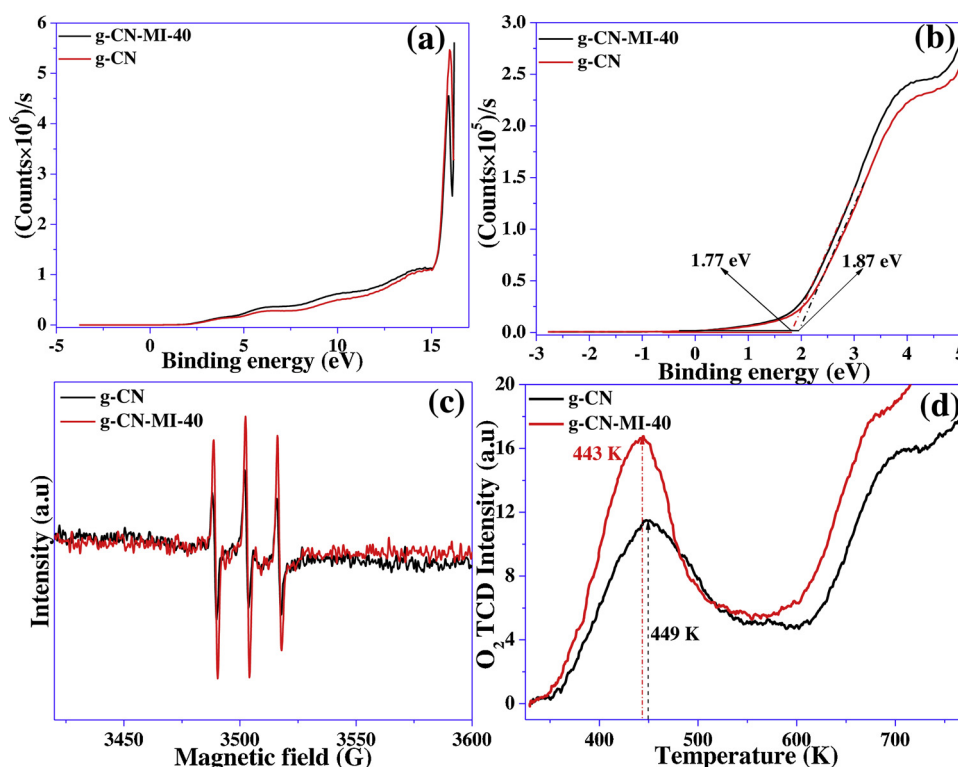


Fig. 10. (a) Ultraviolet photoelectron spectrum (UPS), (b) Corresponding valance band edge spectrum (VBXPS), (c) DMPO-EPR radical trapping experiment for superoxide radical anion, and (d) O_2 -TPD profile of g-CN and g-CN-MI-40 photocatalyst.

for evaluating the effectiveness of the charge carrier's generation upon light illumination [57,75]. As evident from the (i-t) profiles (Fig. 11b), all the photocatalysts coated on FTO exhibit the same signature in their current response under dark and light condition but with a significant difference in the magnitude in their current density. When the light source was illuminated on the catalyst surface, electronic excitation occurred on the semiconductor surface, leading to a pronounced improvement in the output current density which again reverts back to its previous position clearly indicating the smooth photo-reversibility of all the synthesized photocatalysts (Fig. 11b). Further, the obtained current density for g-CN-MI-40 is the highest ($0.054 \mu A/cm^2$) and it is three, two, and 1.5 fold excess than g-CN ($0.018 \mu A/cm^2$), g-CN-MI-30 ($0.032 \mu A/cm^2$), and g-CN-MI-50 ($0.041 \mu A/cm^2$), respectively (Fig. 11b). The difference in the current responses is indicative of the different catalytic behaviour under light illumination. Further to get an insight about the charge carrier migration in the liquid solution and also to obtain the band edge position, Mott-Schottky analysis was performed with bulk g-CN and g-CN-MI-40 by varying the AC frequency under the fixed DC potential of 0.8 V vs. Ag/AgCl under light illumination condition. As shown in (Fig. 11c-d) both the photocatalysts exhibited positive M-S slope under varying AC frequencies which are characteristics of n-type semiconductor [32,57,75]. The flat band potential derived from the X-intercept in the M-S plot is calculated to be -1.05 V (Fig. 11c) and -0.90 V (Fig. 9d) for g-CN and g-CN-MI-40, respectively, against the Ag/AgCl electrode potential at pH = 7 (see supporting information (SI) for the M-S plot and flat band potentials (E_{fb}) estimation).

More importantly, there is a positive shift that occurred in the M-S slope for 2-MI doped g-CN which also matches well with the red-shift in its DRUV-Visible spectrum. For an n-type semiconductor, a reduction in the magnitude of 0.10 V from the flat band potential is considered as the conduction band edge potential [57,75–78]. With the obtained band gap from DRUV-Visible spectrum, the conduction band edge potentials estimated from M-S plot, and the valance band edge potentials derived from the VBXPS, the plausible band edge structure against the

standard potential of Ag/AgCl for g-CN and g-CN-MI-40 can be derived. By taking conduction band edge potentials from the M-S analysis and band gap values from DRUV-Visible spectrum the band structure was constructed and the conduction band edge potentials are estimated to be -0.95 eV and -0.80 eV while the valance band edge potentials are found to be +1.72 eV for both g-CN and g-CN-MI-40, respectively, against the $E^0(Ag/AgCl)$ (Fig. 11c-d). But, taking the valance band edge potential acquired from the VBXPS and band gap values from DRUV-Visible spectrum into the consideration, the conduction band edge potentials are calculated to be -0.90 eV and -0.85 eV while the valance band edge potentials were found to be +1.87 eV and +1.77 eV for g-CN and g-CN-MI-40, respectively (Fig. 10b). Since, a variation in the valance band edge potentials, as well as conduction band edge potentials, are obtained if the VBXPS is considered for the estimation of band edge structure, it seems to be more accurate because both the band edge positions of the semiconductor photocatalyst must be varied from each other as the bulk g-CN was co-doped with carbon and oxygen which will definitely tune the band edge positions as reflected from the VBXPS analysis. Therefore, proceeding with the VBXPS measurements and its estimated band edge potentials, the appropriate band edge structure is schematically presented in Fig. 11f. Notably, the positive shift of the conduction band edge position of g-CN-MI-40 by 0.05 eV from the bulk g-CN is due to the doping impact induced by the oxygen atoms which made the conduction band electrons more reductive for the CO_2 reduction reaction Fig. 11f [32]. Furthermore, electrochemical impedance spectroscopic analysis was carried out for all the photocatalysts which provide useful information regarding the charge transfer resistance properties at the electrode-electrolyte vicinity. All the photocatalysts exhibit similar sinusoidal curve in their EIS profiles which contain a semicircle at a higher frequency and a straight line in the lower frequency zone (Fig. 11e). The semicircle is indicative of the capacitive properties whereas the straight line related to the resistive behaviour [57,75]. The solution resistance (R_s) is the lowest for g-CN-MI-40 (21.5Ω) whereas it is the highest for parent g-CN (28.8Ω) (Inset, Fig. 11e, and Table 1) which indicates that the charge carriers are

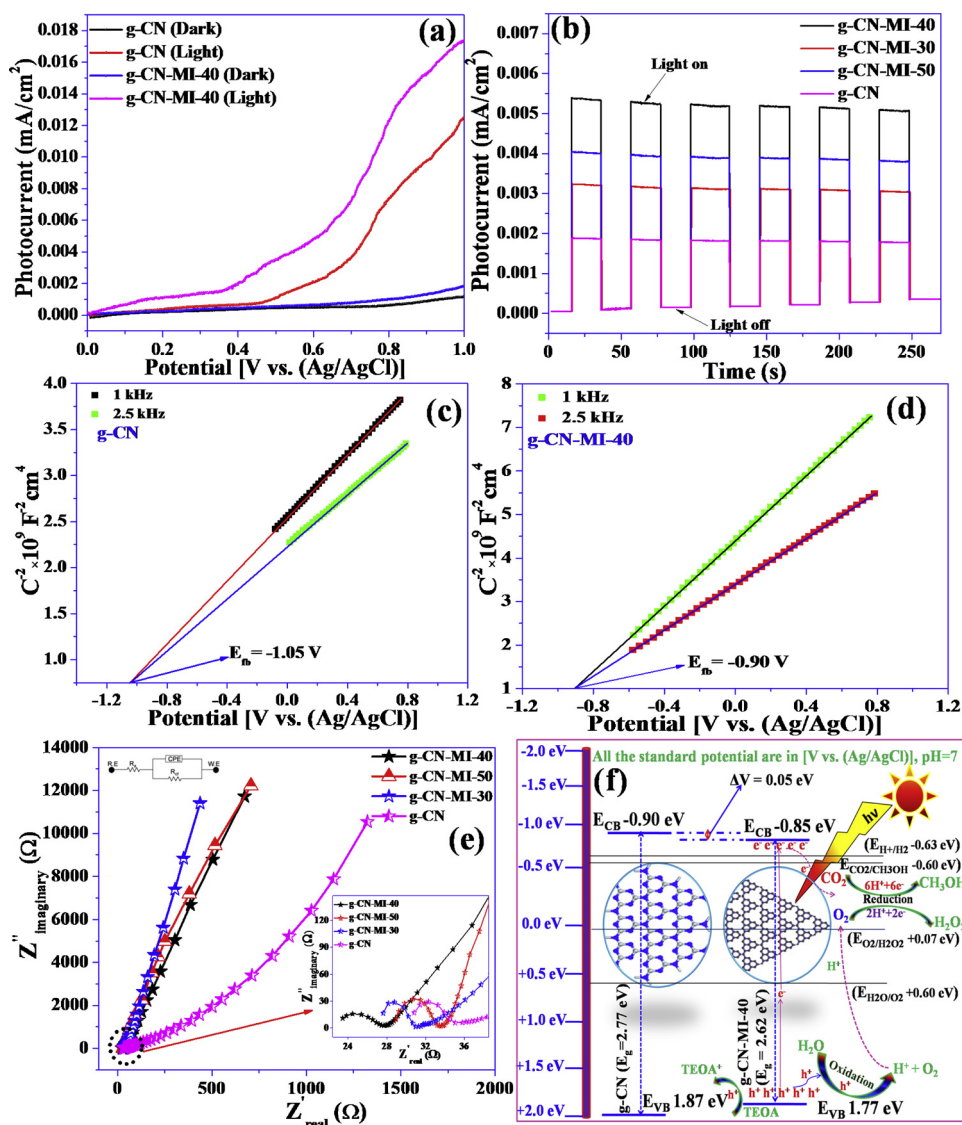


Fig. 11. (a) LSV profiles of g-CN and g-CN-MI-40 under dark and light at a scan rate of 20 mV/s in 0.5 Na₂SO₄ solution (pH = 7), (b) Transient (i-t) profiles of all the photocatalysts measured at bias potential of 0.8 V, (c-d) Mott-Schottky profiles of g-CN and G-CN-MI-40 under different frequencies (1 kHz & 2.5 kHz) at the applied potential of 0.8 V in the light illumination ($\lambda > 420 \text{ nm}$), (e) EIS profiles of the photocatalysts under light (Inset shows the equivalent circuit diagram), (f) Plausible band edge diagram of g-CN and g-CN-MI-40 photocatalyst against standard $E_{\text{Ag/AgCl}}$ at pH = 7.

efficiently transported at the electrode-electrolyte junction upon light illumination over g-CN-MI-40 photocatalyst. Various parameters retrieved from the EIS are summarized in Table 1. This observation further implies that the charge transport properties are modulated after the 2-MI modification over the bulk g-CN.

3.5. Mechanism of photocatalytic CO₂ reduction and H₂O₂ production

After obtaining various information, such as band edge potentials, band gap, CO₂ uptake capacities, and obtained product, it is possible to suggest the plausible mechanism for CO₂ reduction and H₂O₂ production over g-CN based photocatalyst. The conduction band edge potential obtained for g-CN is -0.90 V which is more negative than the standard reduction potential of $E^0(\text{CO}_2/\text{CH}_3\text{OH}) = -0.60 \text{ V}$ (Fig. 11f), $E^0(\text{CO}_2/\text{HCOOH}) = -0.83 \text{ V}$, $E^0(\text{CO}_2/\text{HCHO}) = -0.70 \text{ V}$ vs. $E^0(\text{Ag/AgCl})$ [32]. Therefore, excited electrons have enough potential to reduce the CO₂ to HCOOH, followed by reduction to HCHO, and finally to CH₃OH as the C₁ hydrocarbon fuel in this reaction. The photo-induced holes originated from the valence band oxidized water to produce O₂ and H⁺. While in the next step CO₂ get reduced in a two proton, two-electrons

pathways through a series of intermediates ($\text{CO}_2 + 2\text{H}^+ + 2\text{e}^- = \text{HCOOH} \rightarrow \text{HCHO} \rightarrow \text{CH}_3\text{OH}$) leading to CH₃OH as the final product. This reaction is further favoured by the 2-MI modified g-CN photocatalysts because the thermodynamic constraints are diminished effectively, since the conduction band electrons are more closer to the reduction potential of CO₂/CH₃OH for g-CN-MI-40 ($E_{\text{CB}} = -0.85 \text{ V}$) and valence band holes come more nearer to the standard oxidation potential of H₂O/O₂ ($E_{\text{VB}} = +1.77 \text{ V}$) which in turn accelerated the oxidation reaction to evolve more H⁺ and O₂ from H₂O (Fig. 11f). Selectivity and product distributions depend on many parameters such as reaction environment, the medium of the reaction, nature of the reactant, and most importantly the physicochemical/optoelectronic properties of the involved catalyst. Literature reports suggest that most of the CO₂ photoreduction reactions are being performed in two different conditions at room temperature and under ambient pressure [24]. Between these two sets of CO₂ reduction reaction conditions, one involves H₂O vapour saturated over the photocatalyst immobilized over a plate or silicon wafer and in-situ generated CO₂ gas either through carbamate formation by the reaction between NaHCO₃ and H₂SO₄ or between NaOH and CO₂ gas as the reactants under light irradiation which is referred as

'gas-solid system'. While another one involves CO₂ gas purged on catalyst suspended aqueous solution containing sacrificial agent like TEOA etc. referred as 'suspension system'. In the 'gas-solid system' the main products are found to be CH₄/CO while in the 'suspension system' CH₃OH, HCOOH, HCHO even sometimes C₂H₅OH are obtained [24]. In the 'gas-solid system', the CO₂ is introduced in-situ by its activation in acidic pH condition. Therefore, the preferable products are mostly CH₄/CO. But in the case of 'suspension system', CO₂ gas is directly purged into the catalyst suspended H₂O solution which itself acts as a hole scavengers and supplies the H⁺ and O₂ to the CO₂ molecule which mainly converts to CH₃OH/HCOOH [24]. This is the reason for various CO₂ photoreduction reaction conducted over several g-C₃N₄ catalysts following these two different systems resulted in the variations in the selectivity for different products [24,28]. In our study, the involvement of the 'suspension system' might be the prime reason for the selective production of methanol from CO₂ photoreduction.

In the present photocatalytic system, the H₂O₂ is produced from H₂O and O₂ gas. According to the literature reports, H₂O₂ can be produced sequentially (i) by one-electron reduction of O₂ (O₂ + H⁺ + e⁻ → HO₂) and (ii) in the second step with the assistance of one more electron, it produces H₂O₂ (HO₂ + H⁺ + e⁻ → H₂O₂) [13,27]. In the other way, a concerted 2 electrons reduction can also produce H₂O₂ (O₂ + 2H⁺ + 2e⁻ → H₂O₂) [27]. For the two electrons reduction pathway from O₂ and H₂O the photocatalyst should fulfill two criteria's: (i) The valance band holes must have sufficient positive electrode potential that can oxidize water molecules, and (ii) the valance band electrons should have appropriate band potential for the concerted two electrons reduction of O₂/H₂O₂ [11]. From the band edge structure, it can be seen that both the criteria's are fulfilled by g-CN and g-CN-MI-40 photocatalysts. The valance band position is shifted more closely in the case of 2-MI modified g-CN-MI-40 photocatalyst making this two electrons reduction of di-oxygen more thermodynamically feasible. In addition to that K-L plots obtained from RDE analysis confirms that the number of electrons (n) takes part are 2.42 and 2.26 for g-CN and g-CN-MI-40, respectively (Fig. S11, SI) which are close to the theoretical value of n = 2. More importantly, the LSV profile indicates that both the catalysts are able to oxidize water molecules to produce O₂ (Fig. S12, SI). Further, in the N₂ atmosphere g-CN-MI-40 can also produce H₂O₂ which directly evidence that water oxidation takes place over the catalyst surface which is further reduced by two electrons leading to the H₂O₂ formation. In the presence of O₂ gas, H₂O₂ formation is largely accelerated and finally confirms the two electrons O₂ reduction to produce H₂O₂ which is 100% atom-economic procedure. This phenomenon is further supported by radical scavenging experiment during the H₂O₂ production reaction. In the presence of electron-scavenger (AgNO₃, 0.01 M, 2 mL), the yield of H₂O₂ was significantly suppressed (Fig. 9b). Surprisingly when (h⁺) hole-scavenger (ammonium oxalate 0.01 M, 2 mL) was introduced in the reaction medium yields of H₂O₂ became higher in comparison to the neat reaction condition (Fig. 9b). This is mainly because the quenching of holes diminishes the charge carriers recombination process, minimizes the H₂O₂ decomposition, and electrons are more labile towards the O₂ reduction reaction. Hydroxyl radical scavengers (TBA) also influenced this H₂O₂ formation yield since H₂O₂ can be decomposed to produce (·OH) radicals (Fig. 9b). Therefore, the control radical scavenging experiments further suggest that electrons and hole induced hydroxide radicals are the most dominating species indirectly suggesting the concerted two electrons reduction pathway for H₂O₂ formation reaction from (H₂O + O₂) reaction mixture over the photocatalyst surface. For further obtaining more insight about the reaction mechanism and activity, O₂-TPD and EPR radicals scavenging experiment were conducted to justify our provided reaction mechanism (Fig. 10c-d). In the EPR measurement for H₂O₂ production, DMPO-spin trapping experiment was conducted for both the catalysts (Fig. 10c). The obtained analysis result indicates that three sharp peaks were obtained in the range of (G = 3480–3530) which were completely different from the standard DPMO-O₂⁻ (superoxide

radicals) adduct which ruled out the formation of superoxide radicals by the one-electron reduction of O₂ in the catalytic process [79,80]. Moreover, the reaction was conducted in pure water which also nullifies the proton-coupled electron transfer (PCET) pathway which takes place in the reaction mixture at lower pH (in acidic medium) [81]. In g-C₃N₄ type materials, it was proposed that O₂ is reduced by photo-generated electrons of g-C₃N₄, forming the intermediate '1,4-endoperoxide moieties' across the melem framework of g-C₃N₄, that are subsequently released to form H₂O₂ [11,25,26,82]. The production of H₂O₂ could continue through the hydrolysis of '1,4-endoperoxide species', a well-recognized pathway for the H₂O₂ formation [82]. This '1,4-endoperoxide species' formation was facilitated due to the higher amount of adsorption of O₂ by the g-CN-MI-40 catalyst as evident from its O₂-TPD analysis (Fig. 10d) [15]. Therefore, it implies that the sequential two-step, the one-electron reduction was not the favourable pathway rather the concerted two-electron reduction pathway is governing the H₂O₂ production (O₂ + 2H⁺ + 2e⁻ → H₂O₂) in this study.

3.6. Stability and recyclability of the photocatalyst

High stability and efficient recyclability are the prime parameters in heterogeneous catalysis. In this work, after H₂O₂ production reaction, the catalyst was separated from the reaction mixture using a centrifuge machine operated at 10,000 rpm. The catalyst was washed with acetone and dried at 60 °C for 6 h in a vacuum oven. Before carrying out the next batch of reaction, the catalyst was activated at 100 °C. Similarly, recyclability was also carried in CO₂ photoreduction reaction. In both reactions, only marginal changes in the activities were obtained after 5th cycles (Fig. 12a-b). In order to examine the stability of the doped catalyst (g-CN-MI-40) after conducting the photocatalytic reactions, O 1s high-resolution XPS (HRXPS) spectra for the recovered catalyst after both the reactions was acquired by the XPS measurements and the amount of O present before and after the reaction (in CO₂ photoreduction and H₂O₂ production) in the catalyst is provided in Fig. 12(c-d). The atomic % of O present in the recovered catalyst after CO₂ photoreduction and H₂O₂ production was found to be 2.41% and 2.63% while the fresh catalyst contains (g-CN-MI-40) 2.58% of O (please see and compare Fig. 4e and Fig. 12c-d). During the CO₂ photoreduction, catalyst separation followed by washing and regeneration might be the reason for a little variation in O content in the recovered catalyst than the fresh catalyst. In the H₂O₂ production, the oxygen atomic content is found to be 0.05% higher which might be due to the oxidation of the g-CN-MI-40 catalyst because of the self oxidizing property of H₂O₂ which was *in-situ* produced during the catalytic reaction. These measurements further certify the good cyclic stability of the modified catalyst after these two individual photocatalytic reactions. Catalyst (g-CN-MI-40) recovered after the CO₂ reduction reaction after the 5th cyclic run is of almost similar mass which suggests that carbon present in the g-C₃N₄ was not converted to CH₃OH. Framework stability of the catalyst before and after the reaction further confirms this observation. Moreover, XPS analysis obtained for fresh (47.36% C) and recycled catalyst after 5th (47.25% C) cyclic run provide almost close atomic % of C which evidenced that the framework carbon did not participate in the CO₂ to CH₃OH formation reaction (Fig. S15, SI). Additionally, the retention in the physicochemical properties was also measured with powder XRD, CO₂-TPD, surface survey XPS, and FE-SEM analysis (Fig. S13-S16, SI) which apparently did not exhibit any abrupt changes which confirm the excellent recyclability and stability of the photocatalyst investigated for CO₂ reduction and H₂O₂ production reactions.

4. Conclusion

In summary, a surface-modified C, O co-doped g-C₃N₄ was synthesized and investigated in the photochemical CO₂ reduction and H₂O₂ production. Co-condensation of 2-methyl imidazole eventually

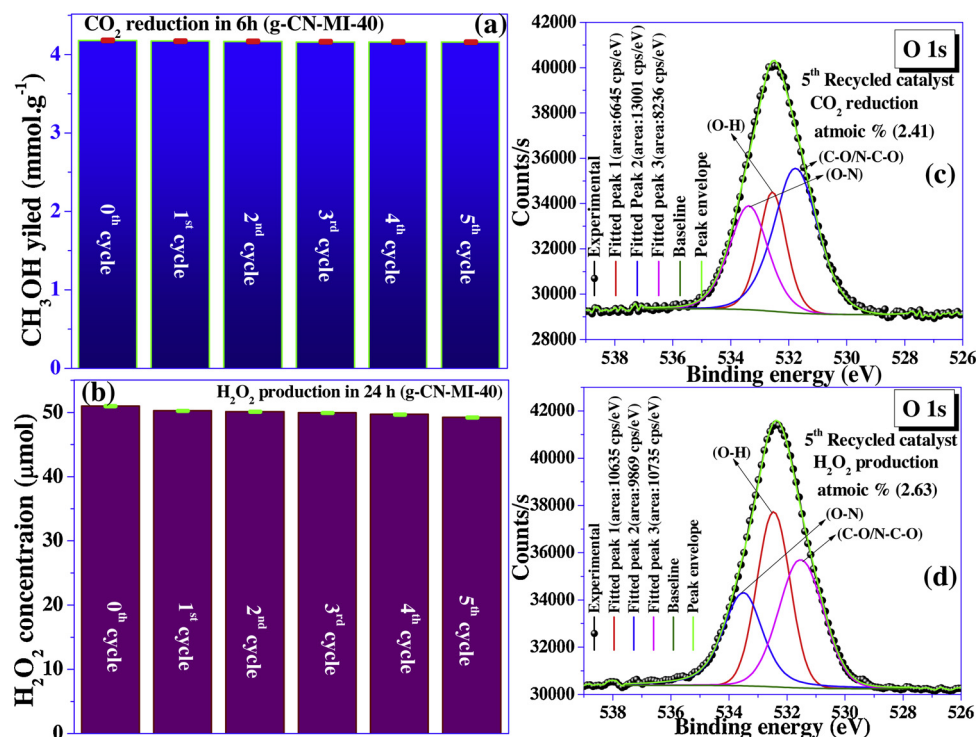


Fig. 12. Recyclability study of (a) CO_2 photoreduction, (b) H_2O_2 production reaction at g-CN-MI-40 photocatalyst for 5 successive cycles (errors bar represent $n = 3$ and ± 0.1), (c) O 1s HRXPS for CO_2 reduction, and (d) H_2O_2 production reaction after the 5th cyclic run.

introduced new carbon and oxygen functionalities which was confirmed from solid-state NMR, XPS, and CO_2 -TPD measurements. The CO_2 photoreduction reaction afforded CH_3OH as the selective product with the yield of 4.18 mmol/g in 6 h for g-CN-MI-40 which was more than bulk g- C_3N_4 (2.8 mmol/g). The H_2O_2 synthesis was investigated in O_2 and H_2O in the absence of any co-catalyst/sacrificial agents and maintaining a 100% atom efficiency that produced 60.3 μmol H_2O_2 in 30 h. The apparent quantum yield was effectively improved from 2.17% (for bulk g- C_3N_4) to 7.23% over the best catalyst g-CN-MI-40 at $\lambda = 420$ nm for H_2O_2 production reaction. The LSV, K-L and DMPO-EPR radical scavenging analysis revealed that it followed the concerted 2 electron reduction pathways for O_2 reduction to produce H_2O_2 . The surface modification of bulk g- C_3N_4 also minimized the preferential one-electron reduction of O_2 to produce (OOH) radicals. The basicity and surface area were also improved which reduced the CO_2 binding energy (7.85 kJ/mol) and therefore CO_2 photoreduction was facilitated after surface modifications. Density functional theory also agreed well with the experimental finding for lowering in the CO_2 adsorption energy after MI modification. Based on the results obtained by the steady-state & time-resolved photoluminescence analysis, Mott-Schottky analysis, valance band XPS, photoelectrochemical measurements, and EIS analysis, it can be concluded that 2-MI modification of g-CN tailored the optoelectronic and photophysical properties of the g-CN-MI photocatalyst. The short-lived lifetime of the charge carriers in the excited states and quenching in the SSPL spectrum indicated the efficacy of the charge carrier's separation. Also, high photocurrent responses under light illumination condition, lower solution resistance, a red-shift in the visible light absorption, favourable band edge alignment were some of the pivotal factors that fine-tune the photocatalytic properties of all the MI-modified g- C_3N_4 photocatalyst. CO_2 -adsorption and CO_2 -TPD indicated that CO_2 uptake capacity, binding energy, and basicity were improved that favoured the CO_2 reduction. Solid-state EPR measurement of the catalysts further suggested that the electronic environment was improved which accelerated both the reduction reaction. So, considering all these factors, it can be concluded that the present photocatalyst could be a potential photocatalyst semiconductor material for

highly efficient CO_2 photoreduction for the selective methanol formation and the atom economic H_2O_2 production from H_2O and O_2 .

Authors contribution

The work plan was demonstrated by SS and RS. RY and AKS contributed in performing the CO_2 reduction reaction and DFT calculation. AK helped in the catalyst synthesis, BET surface area, CO_2 and O_2 -TPD, CO_2 uptake, UV-vis measurements. The manuscript was co-written by SS and RS. All authors have approved the final version of the manuscript.

Declaration of Competing Interest

The authors declare no competing conflict of interest.

Acknowledgements

This work is financially supported by DST-Nano Mission, New Delhi through a research project (SR/NM/NS-1054-2015). SS is thankful to MHRD and CSIR (File No. 09/1005(0024)/2019-EMR-I) and CSIR for providing him with a senior research fellowship. AK and RY are grateful to MHRD, New Delhi and CSIR, New Delhi, respectively, for fellowship. Authors are thankful to CRF-IIT Kharagpur for FE-SEM and HRTEM analysis. We gratefully appreciate the help received from the advanced materials research center (AMRC), IIT Mandi for the XPS, UPS and FE-SEM analysis. Authors also thankful to CIF, IIT Guwahati for TRPL measurements. RS is thankful to Director, IIT Ropar for providing funding in an interdisciplinary project. RS and SS are thankful to JEOL-India, for helping in the solid-state NMR analysis. SS and RS are thankful to the Dean, School of Chemistry, Central University of Hyderabad, India for allowing them to measure the EPR analysis. Authors also acknowledge SAIF-IIT Bombay for the elemental analysis.

Appendix A. Supplementary data

Supplementary material related to this article can be found, in the online version, at doi:<https://doi.org/10.1016/j.apcatb.2019.118054>.

References

- [1] D. Spasiano, R. Marotta, S. Malato, P. Fernandez-Ibanez, I.D. Somma, Solar photocatalysis: materials, reactors, some commercial, and pre-industrialized applications, A Comprehensive Approach, Appl. Catal. B-Environ. 170–171 (2015) 90–123.
- [2] D. Gust, T.A. Moore, A.L. Moore, Solar fuels via artificial photosynthesis, Acc. Chem. Res. 42 (2009) 1890–1898.
- [3] D. Kim, K.K. Sakimoto, D. Hong, P. Yang, Artificial photosynthesis for sustainable fuel and chemical production, Angew. Chem. Int. Ed. 54 (2015) 3259–3266.
- [4] A. Listorti, J. Durrant, J. Barber, Solar to fuel, Nat. Mater. 8 (2009) 929–930.
- [5] X. Li, J. Yu, M. Jaroniec, X. Chen, Co-catalysts for selective photoreduction of CO₂ into solar fuels, Chem. Rev. 119 (2019) 3962–4179.
- [6] X. Liu, S. Inagaki, J. Gong, Heterogeneous molecular systems for photocatalytic CO₂ reduction with water oxidation, Angew. Chem. Int. Ed. 55 (2016) 14924–14950.
- [7] T. Inoue, A. Fujishima, S. Konishi, K. Honda, Photoelectrocatalytic reduction of carbon dioxide in aqueous suspensions of semiconductor powders, Nature 277 (1979) 637–638.
- [8] B.E. Solsona, J.K. Edwards, P. Landon, A.F. Carley, A. Herzog, C.J. Kiely, G.J. Hutchings, Direct synthesis of hydrogen peroxide from H₂ and O₂ using Al₂O₃ supported Au-Pd catalysts, Chem. Mater. 18 (2006) 2689–2695.
- [9] F. Sandelin, P. Oinas, T. Salmi, J. Paloniemi, H. Haario, Kinetics of the recovery of active anthraquinones, Ind. Eng. Chem. Res. 45 (2006) 986–992.
- [10] C. Kormann, D.W. Bahnemann, M.R. Hoffmann, Photocatalytic production of H₂O₂ and organic peroxides in aqueous suspensions of TiO₂, ZnO, and desert sand, Environ. Sel. Technol. 22 (1988) 798–806.
- [11] Y. Shiraishi, S. Kanazawa, Y. Kofuji, H. Sakamoto, S. Ichikawa, S. Tanaka, T. Hirai, Sunlight-driven hydrogen peroxide production from water and molecular oxygen by metal-free photocatalysts, Angew. Chem. Int. Ed. 53 (2014) 13454–13459.
- [12] F. Feng, W. Yang, S. Gao, C. Sun, Q. Li, Postillumination activity in a single-phase photocatalyst of Mo-doped TiO₂ nanotube array from its photocatalytic “memory”, ACS Sustainable Chem. Eng. 6 (2018) 6166–6174.
- [13] S. Thakur, T. Kshetri, N.H. Kim, J.H. Lee, Sunlight-driven sustainable production of hydrogen peroxide using a CdS-Graphene hybrid photocatalyst, J. Catal. 345 (2017) 78–86.
- [14] H. Kim, J. Lim, S. Lee, H.H. Kim, C. Lee, J. Lee, W. Choi, Spontaneous generation of H₂O₂ and hydroxyl radical through O₂ reduction on copper phosphide under ambient aqueous condition, Environ. Sci. Technol. 53 (2019) 2918–2925.
- [15] S. Zhao, X. Zhao, S. Ouyang, Y. Zhu, Polyoxometalates covalently combined with graphitic carbon nitride for photocatalytic hydrogen peroxide production, Catal. Sci. Technol. 8 (2018) 1686–1695.
- [16] H. Kim, Y. Choi, S. Hu, W. Choi, J.H. Kim, Photocatalytic hydrogen peroxide production by anthraquinone-augmented polymeric carbon nitride, Appl. Catal. B-Environ. 229 (2018) 121–129.
- [17] Y. Isaka, Y. Kawase, Y. Kuwahara, K. Mori, H. Yamashita, Two-phase system utilizing hydrophobic metal-organic-frameworks (MOFs) for photocatalytic synthesis of hydrogen peroxide, Angew. Chem. Int. Ed. 131 (2019) 5456–5460.
- [18] S. Zhao, T. Guo, X. Li, T. Xu, B. Yang, X. Zhao, Carbon nanotubes covalent combined with graphitic carbon nitride for photocatalytic hydrogen peroxide production under visible light, Appl. Catal. B-Environ. 224 (2018) 725–732.
- [19] Y. Zhao, Y. Wei, X. Wu, H. Zheng, Z. Zhao, J. Liu, J. Li, Graphene-wrapped Pt/TiO₂ photocatalysts with enhanced photogenerated charges separation and reactant adsorption for high selective photoreduction of CO₂ to CH₄, Appl. Catal. B-Environ. 226 (2018) 360–372.
- [20] J. Jiao, Y. Wei, Y. Zhao, Z. Zhao, A. Duan, J. Liu, Y. Pang, J. Li, G. Jiang, Y. Wang, AuPd/3DOM-TiO₂ catalysts for photocatalytic reduction of CO₂: high efficient separation of photogenerated charge carriers, Appl. Catal. B-Environ. 209 (2017) 228–239.
- [21] Y. Wei, X. Wu, Y. Zhao, L. Wang, Z. Zhao, X. Huang, J. Liu, J. Li, Efficient photocatalysts of TiO₂ nanocrystals-supported PtRu alloy nanoparticles for CO₂ reduction with H₂O: synergistic effect of Pt-Ru, Appl. Catal. B-Environ. 236 (2018) 445–457.
- [22] P. Niu, Y. Yang, J. Yu, G. Liu, H.-M. Cheng, Switching the selectivity of the photoreduction reaction of carbon dioxide by controlling the band structure of a g-C₃N₄ photocatalyst, Chem. Commun. (Camb.) 50 (2014) 10837–10840.
- [23] Y. Yang, X. Wang, Photocatalytic CO₂ conversion by polymeric carbon nitrides, Chem. Commun. (Camb.) 54 (2018) 5674–5687.
- [24] Z. Sun, H. Wang, Z. Wu, L. Wang, g-C₃N₄ based composite photocatalysts for photocatalytic CO₂ reduction, Catal. Today 300 (2018) 160–172.
- [25] Y. Shiraishi, Y. Kofuji, H. Sakamoto, S. Tanaka, S. Ichikawa, T. Hirai, Effects of surface defects on photocatalytic H₂O₂ production by mesoporous graphitic carbon nitride under visible light irradiation, ACS Catal. 5 (2015) 3058–3066.
- [26] Y. Kofuji, Y. Isobe, Y. Shiraishi, H. Sakamoto, S. Tanaka, S. Ichikawa, T. Hirai, Carbon nitride aromatic diimide graphene nanohybrids: metal-free photocatalysts for solar-to-hydrogen peroxide energy conversion with 0.2% efficiency, J. Am. Chem. Soc. 138 (2016) 10019–10025.
- [27] S. Kim, G. Moon, H. Kim, Y. Mun, P. Zhang, J. Lee, W. Choi, Selective charge transfer to dioxygen on KPF₆-modified carbon nitride for photocatalytic synthesis of H₂O₂ under visible light, J. Catal. 357 (2018) 51–58.
- [28] S. Ye, R. Wang, M.-Z. Wu, Y.-P. Yuan, A review on g-C₃N₄ for photocatalytic water splitting and CO₂ reduction, Appl. Surf. Sci. 358 (2015) 15–27.
- [29] J.K. Stolarczyk, S. Bhattacharyya, L. Polavarapu, J. Feldmann, Challenges and prospects in solar water splitting and CO₂ reduction with inorganic and hybrid nanostructures, ACS Catal. 8 (2018) 3602–3635.
- [30] K. Wang, Q. Li, B. Liu, B. Cheng, W. Ho, J. Yu, Sulfur-doped g-C₃N₄ with enhanced photocatalytic CO₂-reduction performance, Appl. Catal. B-Environ. 176–177 (2015) 44–52.
- [31] Z. Zhu, H. Pan, M. Murugananthan, J. Gong, Y. Zhang, Visible light-driven photocatalytically active g-C₃N₄ material for enhanced generation of H₂O₂, Appl. Catal. B-Environ. 232 (2018) 19–25.
- [32] J. Fu, B. Zhu, C. Jiang, B. Cheng, W. You, J. Yu, Hierarchical porous O-doped g-C₃N₄ with enhanced photocatalytic CO₂ reduction activity, Small 13 (1–9) (2017) 1603938.
- [33] B. Liu, L. Ye, R. Wang, J. Yang, Y. Zhang, R. Guan, L. Tian, X. Chen, Phosphorus-doped graphitic carbon nitride nanotubes with amorphous surface for efficient CO₂ capture, enhanced photocatalytic activity, and product selectivity, ACS Appl. Mater. Interfaces 10 (2018) 4001–4009.
- [34] E.M. Dias, K.C. Christoforidis, L. Francàs, C. Petit, Tuning thermally treated graphitic carbon nitride for H₂ evolution and CO₂ photoreduction: the effects of material properties and mid-gap states, ACS Appl. Energy Mater. 1 (2018) 6524–6534.
- [35] Y. Li, R. Jin, Y. Xing, J. Li, S. Song, X. Liu, M. Li, R. Jin, Macroscopic foam-like holey ultrathin g-C₃N₄ nanosheets for drastic improvement of visible-light photocatalytic activity, Adv. Energy Mater. 6 (1–5) (2016) 1601273.
- [36] D. Vidyasagar, N. Manwar, A. Gupta, S.G. Ghugal, S.U. Umare, R. Boukherroub, Phenyl-grafted carbon nitride semiconductor for photocatalytic CO₂-reduction and rapid degradation of organic dyes, Catal. Sci. Technol. 9 (2019) 822–832.
- [37] Y. Kofuji, S. Ohkita, Y. Shiraishi, H. Sakamoto, S. Tanaka, S. Ichikawa, T. Hirai, Melitic triimide-doped carbon nitride as sunlight-driven photocatalysts for hydrogen peroxide production, ACS Sustainable Chem. Eng. 5 (2017) 6478–6485.
- [38] Y. Kofuji, S. Ohkita, Y. Shiraishi, H. Sakamoto, S. Tanaka, S. Ichikawa, T. Hirai, Graphitic carbon nitride doped with biphenyl diimide: efficient photocatalyst for hydrogen peroxide production from water and molecular oxygen by sunlight, ACS Catal. 6 (2016) 7021–7029.
- [39] H. Kim, S. Gim, T.W. Jeon, H. Kim, W. Choi, Distorted carbon nitride structure with substituted benzene moieties for enhanced visible light photocatalytic activities, ACS Appl. Mater. Interfaces 9 (2017) 40360–40368.
- [40] A. Torres-Pinto, M.J. Sampaio, C.G. Silva, J.L. Faria, A.M.T. Silva, Metal-free carbon nitride photocatalysis with in situ hydrogen peroxide generation for the degradation of aromatic compounds, Appl. Catal. B-Environ. 252 (2019) 128–137.
- [41] X. She, L. Liu, H. Ji, Z. Mo, Y. Li, L. Huang, D. Du, H. Xu, H. Li, Template-free synthesis of 2D porous ultrathin non metal-doped g-C₃N₄ nanosheets with highly efficient photocatalytic H₂ evolution from water under visible light, Appl. Catal. B-Environ. 187 (2016) 144–153.
- [42] J.-W. Zhang, G. S. N. Mahmood, L. Pan, X. Zhang, J.-J. Zou, Oxygen-doped nanoporous carbon nitride via water-based homogeneous supramolecular assembly for photocatalytic hydrogen evolution, Appl. Catal. B-Environ. 221 (2018) 9–16.
- [43] C. Liu, H. Huang, W. Cui, F. Dong, Y. Zhang, Band structure engineering and efficient charge transport in oxygen substituted g-C₃N₄ for superior photocatalytic hydrogen evolution, Appl. Catal. B-Environ. 230 (2018) 115–124.
- [44] J. Wu, N. Li, X.-H. Zhang, H.-B. Fang, Y.-Z. Zheng, X. Tao, Heteroatoms binary-doped hierarchical porous g-C₃N₄ nanobelts for remarkably enhanced visible-light-driven hydrogen evolution, Appl. Catal. B-Environ. 226 (2018) 61–70.
- [45] Y. Jiang, Z. Sun, C. Tang, Y. Zhou, L. Zeng, L. Huang, Enhancement of photocatalytic hydrogen evolution activity of porous oxygen doped g-C₃N₄ with nitrogen defects induced by changing electron transition, Appl. Catal. B-Environ. 240 (2019) 30–38.
- [46] Y. Huang, D. Li, Z. Fang, R. Chen, B. Luo, W. Shi, Controlling carbon self-doping site of g-C₃N₄ for highly enhanced visible light-driven hydrogen evolution, Appl. Catal. B-Environ. 254 (2019) 128–134.
- [47] Q. Liu, J. Shen, X. Yu, X. Yang, W. Liu, J. Yang, H. Tang, H. Xu, H. Li, Y. Li, J. Xu, Unveiling the origin of boosted photocatalytic hydrogen evolution in simultaneously (S, P, O)-codoped and exfoliated ultrathin g-C₃N₄ Nanosheets, Appl. Catal. B-Environ. 248 (2019) 84–94.
- [48] S. Samanta, R. Srivastava, A novel method to introduce acidic and basic bifunctional sites in graphitic carbon nitride for sustainable catalysis: cycloaddition, esterification, and transesterification reactions, Sustain. Energy Fuels 1 (2017) 1390–1404.
- [49] S. Samanta, S. Martha, K. Parida, Facile synthesis of Au/g-C₃N₄ nanocomposites: an inorganic/organic hybrid plasmonic photocatalyst with enhanced hydrogen gas evolution under visible-light irradiation, ChemCatChem 6 (2014) 1453–1462.
- [50] M. Li, L. Zhang, X. Fan, M. Wu, Y. Du, M. Wang, Q. Kong, L. Zhang, J. Shi, Dual synergistic effects in MoS₂/pyridine-modified g-C₃N₄ composite for highly active and stable photocatalytic hydrogen evolution under visible light, Appl. Catal. B-Environ. 190 (2016) 36–43.
- [51] Y. Wang, H. Wang, F. Chen, F. Cao, X. Zhao, S. Meng, Y. Cui, Facile synthesis of Oxygen doped carbon nitride hollow microsphere for photocatalysis, Appl. Catal. B-Environ. 206 (2017) 417–425.
- [52] N. Tian, Y. Zhang, Li X, K. Xiao, X. Du, F. Dong, G.I.N. Waterhouse, T. Zhang, H. Huang, Precursor-reforming protocol to 3D mesoporous g-C₃N₄ established by ultrathin self-doped nanosheets for superior hydrogen evolution, Nano Energy 38 (2017) 72–81.
- [53] X.J. She, J.J. Wu, J. Zhong, H. Xu, Y.C. Yang, R. Vajtai, J. Lou, Y. Liu, D.L. Du, H.M. Li, P.M. Ajayan, Oxygenated monolayer carbon nitride for excellent photocatalytic hydrogen evolution and external quantum efficiency, Nano Energy 27 (2016) 138–146.
- [54] S. Sun, J. Li, J. Cui, X. Gou, Q. Yang, S. Liang, Z. Yang, J. Zhang, Constructing oxygen-doped g-C₃N₄ nanosheets with an enlarged conductive band edge for

- enhanced visible-light-driven hydrogen evolution, *Inorg. Chem. Front.* 5 (2018) 1721–1727.
- [55] J.H. Li, B. Shen, Z.H. Hong, B.Z. Lin, B.F. Gao, Y.L. Chen, A facile approach to synthesize novel oxygen-doped g-C₃N₄ with superior visible-light photoreactivity, *Chem. Commun. (Camb.)* 48 (2012) 12017–12019.
- [56] S. Samanta, R. Srivastava, Thermal catalysis vs. photocatalysis: a case study with FeVO₄/g-C₃N₄ nanocomposites for the efficient activation of aromatic and benzylic C-H bonds to oxygenated products, *Appl. Catal. B-Environ.* 218 (2017) 621–636.
- [57] S. Samanta, B. Satpati, R. Srivastava, Unraveling the impact of the Pd nanoparticle@BiVO₄/S-CN heterostructure on the photo-physical & opto-electronic properties for enhanced catalytic activity in water splitting and one-pot three-step tandem reaction, *Nanoscale Adv.* 1 (2019) 1395–1412.
- [58] J. Fu, S. Cao, J. Yu, J. Low, Y. Lei, Enhanced photocatalytic CO₂-reduction activity of electrospon mesoporous TiO₂ nanofibers by solvothermal treatment, *Dalton Trans.* 43 (2014) 9158–9165.
- [59] T. Zhang, C. Wang, S. Liu, J.-L. Wang, W. Lin, A biomimetic copper water oxidation catalyst with low overpotential, *J. Am. Chem. Soc.* 136 (2014) 273–281.
- [60] X. Ma, Y. Lv, J. Xu, Y. Liu, R. Zhang, Y. Zhu, A strategy of enhancing the photo-activity of g-C₃N₄ via doping of nonmetal elements: a first-principles study, *J. Phys. Chem. C* 116 (2012) 23485–23493.
- [61] J. Qin, S. Wang, H. Ren, Y. Hou, X. Wang, Photocatalytic reduction of CO₂ by graphitic carbon nitride polymers derived from urea and barbituric acid, *Appl. Catal. B-Environ.* 179 (2015) 1–8.
- [62] G. Dong, L. Zhang, Porous structure dependent photoreactivity of graphitic carbon nitride under visible light, *J. Mater. Chem.* 22 (2012) 1160–1166.
- [63] K. Wang, J. Fu, Y. Zheng, Insights into photocatalytic CO₂ reduction on C₃N₄: strategy of simultaneous B, K co-doping and enhancement by N vacancies, *Appl. Catal. B-Environ.* 254 (2019) 270–280.
- [64] Y. Wang, Q. Xia, X. Bai, Z. Ge, Q. Yang, C. Yin, S. Kang, M. Dong, Xi Li, Carbothermal activation synthesis of 3D porous g-C₃N₄/carbon nanosheets composite with superior performance for CO₂ photoreduction, *Appl. Catal. B-Environ.* 239 (2018) 196–203.
- [65] L. Lina, C. Hou, X. Zhang, Y. Wang, Y. Chen, T. He, Highly efficient visible-light driven photocatalytic reduction of CO₂ over g-C₃N₄ nanosheets/tetra(4-carboxyphenyl)porphyrin iron(III) chloride heterogeneous catalysts, *Appl. Catal. B-Environ.* 221 (2018) 312–319.
- [66] N. Tian, K. Xiao, Y. Zhang, X. Lu, L. Ye, P. Gao, T. Ma, H. Huang, Reactive sites rich porous tubular yolk-shell g-C₃N₄ via precursor recrystallization mediated microstructure engineering for photoreduction, *Appl. Catal. B-Environ.* 253 (2019) 196–205.
- [67] Z. Mo, X. Zhu, Z. Jiang, Y. Song, D. Liu, H. Li, X. Yang, Y. She, Y. Lei, S. Yuan, H. Li, L. Song, Q. Yan, H. Xu, Porous nitrogen-rich g-C₃N₄ nanotubes for efficient photocatalytic CO₂ reduction, *Appl. Catal. B-Environ.* 256 (2019) 117854.
- [68] K. Maeda, R. Kuriki, M. Zhang, X. Wang, O. Ishitani, The effect of the pore-wall structure of carbon nitride on photocatalytic CO₂ reduction under visible light, *J. Mater. Chem. A Mater. Energy Sustain.* 2 (2014) 15146–15151.
- [69] J. Mao, T. Peng, X. Zhang, K. Li, L. Ye, L. Zan, Effect of graphitic carbon nitride microstructures on the activity and selectivity of photocatalytic CO₂ reduction under visible light, *Catal. Sci. Technol.* 3 (2013) 1253–1260.
- [70] N.D. Shcherban, S.M. Filonenko, M.L. Ovcharov, A.M. Mishura, M.A. Skoryk, A. Aho, D.Y. Murzin, Simple method for preparing of sulphur-doped graphitic carbon nitride with superior activity in CO₂ photoreduction, *Chem. Select* 1 (2016) 4987–4993.
- [71] R. Yadav, V. Amoli, J. Singh, M.K. Tripathi, P. Bhanja, A. Bhaumik, A.K. Sinha, Plasmonic gold deposited on mesoporous Ti_xSi_{1-x}O₂ with isolated Si in lattice: an excellent photocatalyst for photocatalytic conversion CO₂ into methanol under visible light irradiation, *J. CO₂ Utilization* 27 (2018) 11–21.
- [72] Y.Y. Liu, B.B. Huang, Y. Dai, X.Y. Zhang, X.Y. Qin, M.H. Jiang, M.H. Whangbo, Selective ethanol formation from photocatalytic reduction of carbon dioxide in water with BiVO₄ photocatalyst, *Catal. Commun.* 11 (2009) 210–213.
- [73] X. Li, C. Chen, J. Zhao, Mechanism of photodecomposition of H₂O₂ on TiO₂ surfaces under visible light irradiation, *Langmuir* 17 (2001) 4118–4122.
- [74] R. Zhou, Y. Zheng, M. Jaroniec, S.-Z. Qiao, Determination of the electron transfer number for the oxygen reduction reaction: from theory to experiment, *ACS Catal.* 6 (2016) 4720–4728.
- [75] S. Samanta, S. Khilari, R. Srivastava, Stimulating the visible-light catalytic activity of Bi₂MoO₆ nanoplates by embedding carbon dots for the efficient oxidation, cascade reaction, and photoelectrochemical O₂ evolution, *ACS Appl. Nano Mater.* 1 (2018) 426–441.
- [76] X. Hao, D. X. X. Wang, S. Zhai, H. Ma, X. Zhang, Controllable electrostatic self-assembly of sub-3 nm graphene quantum dots incorporated into mesoporous Bi₂MoO₆ frameworks: efficient physical and chemical simultaneous co-catalysis for photocatalytic oxidation, *J. Mater. Chem. A Mater. Energy Sustain.* 4 (2016) 8298–8307.
- [77] A. Ishikawa, T. Takata, J.N. Kondo, M. Hara, H. Kobayashi, K. Domen, Oxysulfide Sm₂Ti₂S₂O₅ as a stable photocatalyst for water oxidation and reduction under visible light irradiation ($\lambda \leq 650$ nm), *J. Am. Chem. Soc.* 124 (2002) 13547–13553.
- [78] J. Yang, X.H. Wang, X.L. Zhao, J. Dai, S.R. Mo, Synthesis of uniform Bi₂WO₆-reduced graphene oxide nanocomposites with significantly enhanced photocatalytic reduction activity, *J. Phys. Chem. C* 119 (2015) 3068–3078.
- [79] P. Xia, B. Cheng, J. Jiang, H. Tang, Localized π -conjugated structure and EPR investigation of g-C₃N₄ photocatalyst, *Appl. Surf. Sci.* 487 (2019) 335–342.
- [80] D. Dvoranova, Z. Barbierikova, M. Mazur, E.I. Garcia-Lopez, G. Marci, K. Lušpai, V. Brezova, EPR investigations of polymeric and H₂O₂-modified C₃N₄-based photocatalysts, *J. Photochem. Photobiol. A: Chem.* 375 (2019) 100–113.
- [81] G. Moon, W. Kim, A.D. Bokare, N. Sung, W. Choi, Solar production of H₂O₂ on reduced graphene oxide-TiO₂ hybrid photocatalysts consisting of earth-abundant elements only, *Energy Environ. Sci.* 7 (2014) 4023–4028.
- [82] W.-C. Hou, Y.-S. Wang, Photocatalytic generation of H₂O₂ by graphene oxide in organic electron donor-free condition under sunlight, *ACS Sustainable Chem. Eng.* 5 (2017) 2994–3001.